

**Transient Liquid Phase Brazing of Nickel to Alumina
Using Nickel-Titanium Interlayers**

by

Stephen M. Wilson

ProQuest Number: 10794371

All rights reserved

INFORMATION TO ALL USERS

The quality of this reproduction is dependent upon the quality of the copy submitted.

In the unlikely event that the author did not send a complete manuscript and there are missing pages, these will be noted. Also, if material had to be removed, a note will indicate the deletion.



ProQuest 10794371

Published by ProQuest LLC (2018). Copyright of the Dissertation is held by the Author.

All rights reserved.

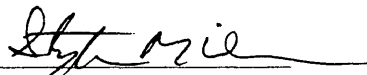
This work is protected against unauthorized copying under Title 17, United States Code
Microform Edition © ProQuest LLC.

ProQuest LLC.
789 East Eisenhower Parkway
P.O. Box 1346
Ann Arbor, MI 48106 – 1346


A thesis submitted to the Faculty and Board of Trustees of the Colorado School of Mines in partial fulfillment of the requirements for the degree of Master of Science (Metallurgical and Materials Engineering)

Golden, Colorado

Date 9/24/98


Signed: 
Stephen M. Wilson

ARTHUR LAKES LIBRARY
COLORADO SCHOOL OF MINES
GOLDEN, CO 80401

Approved: 
Thesis advisor
Dr. G. R. Edwards

Golden, Colorado

Date 9/24/98


Dr. J. J. Moore
Professor and Head,
Department of Metallurgical
and Materials Engineering

Abstract

In this study, the joining of alumina to nickel by transient liquid phase brazing using nickel-titanium interlayers was analyzed. This process has several advantages over the widely used copper-silver-titanium brazing method. The copper-titanium system exhibits several brittle intermetallic compounds that reduce the strength of the joint. The nickel-titanium system has only a small number of intermetallic compounds, one of which is NiTi, a phase known to be a ductile banded martensite and the basis for numerous shape memory alloys. The nickel-titanium system also has higher solidus and liquidus temperatures that, while they require higher bonding temperatures, allow for higher service temperatures. Transient liquid phase brazing allows brazing to occur at temperatures below the melting point of pure titanium and nickel.

Samples were subjected to four-point bend testing to determine mechanical properties, as well as analysis with a scanning electron microscope. Joint strengths measured as high as 26 ksi (180 MPa), a value equivalent to approximately 45 percent of the bend strength of pure monolithic alumina. An analysis of the fracture surfaces showed that each sample fractured within the ceramic material, evidence of the presence of residual stresses within the joint.

A kinetic analysis of the bond formation was possible using the data generated by SEM analysis. The formation of NiTi was seen to happen very rapidly, during the

heating to the brazing temperature. As the brazing cycle progressed, the NiTi layer became richer in nickel, forming first a liquid then solidifying to form Ni₃Ti. The formation of Ni₃Ti was seen to be parabolic in nature. Further analysis of this growth resulted in the determination of an apparent activation energy of 130 kJ/mol.

Table of Contents

| | |
|--|-----|
| Abstract | iii |
| List of Figures | vii |
| Acknowledgments | x |
| I. Introduction | 1 |
| A. Joining Applications | 3 |
| B. Joining Methods | 4 |
| C. Important Factors in Brazing | 5 |
| II. Literature Review | 7 |
| A. Wetting and Spreading | 7 |
| 1. General Theory | 8 |
| 2. Measurement of Contact Angle | 10 |
| 3. Non-reactive systems | 13 |
| 4. Reactive Systems | 13 |
| B. Reaction Layer Formation | 17 |
| 1. Ceramic-Metal Bonding | 17 |
| 2. Possible Products | 20 |
| 3. Thickening Kinetics | 25 |
| C. Current Technology in Metal/Ceramic Brazing | 43 |
| 1. General Metal/Ceramic Brazing | 43 |
| 2. Transient Liquid Phase Brazing | 45 |
| III. Experimental Procedure | 53 |
| A. Materials Used | 53 |
| B. Creation of Samples | 54 |
| C. Mechanical Testing | 57 |
| D. Scanning Electron Microscope Analysis | 59 |
| IV. Results | 61 |

| | |
|---|----|
| A. Mechanical Testing | 61 |
| B. Compositional Profiles Microscopy. | 68 |
| C. Fracture Surface Analysis | 70 |
| V. Discussion | 71 |
| A. Microstructure-Strength Correlation | 71 |
| B. Fracture Behavior | 72 |
| C. Bond Development | 74 |
| D. Kinetic Analysis of Ni ₃ Ti | 77 |
| VI. Conclusions | 88 |
| VII. References | 89 |

ARTHUR LAKES LIBRARY
 COLORADO SCHOOL OF MINES
 GOLDEN, CO 80401

List of Figures

| | | |
|-------------|---|----|
| Figure 1.1: | Nickel-titanium phase diagram (Massalski [1]) | 2 |
| Figure 2.1: | Sessile drop schematic diagram illustrating contact angle and relevant interfacial energies | 9 |
| Figure 2.2: | Schematic illustration of wetting in a reactive system | 16 |
| Figure 2.3: | Linear relationship between the work of adhesion of different liquid metals on alumina and the electron density, n_{ws} [22] | 21 |
| Figure 2.4: | Simplified model for diffusion controlled oxidation [66] | 28 |
| Figure 2.5: | Diagram of scale formation according to Wagner's model [66] | 31 |
| Figure 2.6: | Four-point bend test results of the brazed joints by Cu-X alloys [77] | 46 |
| Figure 2.7: | Schematic showing different stages during TLP bonding, where T_B is the bonding temperature and T_M is the melting point of the filler metal [82] | 49 |
| Figure 3.1: | Sample configuration used in TLP brazing experiments with nickel-titanium interlayers | 55 |
| Figure 3.2: | Thermal cycle used in TLP brazing of alumina to nickel | 56 |
| Figure 3.3: | Four-point bend sample showing relevant dimensions | 58 |
| Figure 3.4: | Micrograph of nickel-alumina interface and interlayer region, showing trace of SEM scan | 60 |
| Figure 4.1: | Four-point bend strength versus isothermal holding time for nickel/alumina joints with titanium-40 weight percent nickel interlayers at 1150°C | 62 |

| | | |
|-------------|---|----|
| Figure 4.2: | Four-point bend strength versus isothermal holding time for nickel/alumina joints with titanium-30 weight percent nickel interlayers at 1150°C | 63 |
| Figure 4.3: | Four-point bend strength versus isothermal holding time for nickel/alumina joints with titanium-40 weight percent nickel interlayers at 1200°C | 64 |
| Figure 4.4: | Four-point bend strength versus isothermal holding time for nickel/alumina joints with titanium-30 weight percent nickel interlayers at 1200°C | 65 |
| Figure 4.5: | Four-point bend strength of nickel/alumina TLP brazed samples with titanium-30 weight percent nickel interlayers as a function of V_{Ni_3Ti}/V_{NiTi} | 66 |
| Figure 4.6: | Four-point bend strength of nickel/alumina TLP brazed samples with titanium-40 weight percent nickel interlayers as a function of V_{Ni_3Ti}/V_{NiTi} | 67 |
| Figure 4.7: | Representative compositional profile created with data from SEM analysis of nickel/alumina TLP brazed joints | 69 |
| Figure 5.1: | Schematic of cooling of ceramic/metal brazed joint from brazing temperature to room temperature | 73 |
| Figure 5.2: | Nickel-titanium phase diagram with compositional changes as a result of the brazing cycle plotted | 75 |
| Figure 5.3: | Thickness of Ni ₃ Ti layer versus time ^{1/2} for nickel/alumina samples with titanium-30 weight percent nickel interlayers brazed at 1150°C | 78 |
| Figure 5.4: | Thickness of Ni ₃ Ti layer versus time ^{1/2} for nickel/alumina samples with titanium-30 weight percent nickel interlayers brazed at 1200°C | 79 |
| Figure 5.5: | Thickness of Ni ₃ Ti layer versus time ^{1/2} for nickel/alumina samples with titanium-30 weight percent nickel interlayers brazed at 1250°C | 80 |

| | | |
|--------------|---|----|
| Figure 5.6: | Thickness of Ni ₃ Ti layer versus time ^{1/2} for nickel/alumina samples with titanium-40 weight percent nickel interlayers brazed at 1150°C | 81 |
| Figure 5.7: | Thickness of Ni ₃ Ti layer versus time ^{1/2} for nickel/alumina samples with titanium-40 weight percent nickel interlayers brazed at 1200°C | 82 |
| Figure 5.8: | Thickness of Ni ₃ Ti layer versus time ^{1/2} for nickel/alumina samples with titanium-40 weight percent nickel interlayers brazed at 1250°C | 83 |
| Figure 5.9: | Temperature dependence of the reaction rate constant, K: logarithm of K as a function of inverse absolute temperature for the growth of Ni ₃ Ti in nickel/alumina TLP brazed joints with titanium-30 weight percent nickel interlayers | 86 |
| Figure 5.10: | Temperature dependence of the reaction rate constant, K: logarithm of K as a function of inverse absolute temperature for the growth of Ni ₃ Ti in nickel/alumina TLP brazed joints with titanium-40 weight percent nickel interlayers | 87 |

Acknowledgments

I would like to thank my advisor, Dr. Glen Edwards, for providing the opportunity to continue my education, for his continual encouragement and for his seemingly endless patience. I would also like to acknowledge the help of the faculty and staff of the Metallurgy department particularly S. Pawelka, S. Donalson, and R. McGrew.

I owe an enormous debt of gratitude to my fellow graduate students, both past and present, for their support, encouragement, and insights, especially D. Javernick, M. Clark, K. Johnson, B. Mulac, and M. Rowe.

I would also like to thank Dr. Alan Meier for his help, without which this project would not have been possible, and the Office on Naval Research for the funding of this project.

Last of all, I would like to thank my friends and family for their support and encouragement during my education and for never letting me give up.

I Introduction

Advanced ceramics are finding new applications in many areas including the aerospace, automotive, nuclear and electronics industries. However, cost considerations or additional mechanical, electrical or thermal property requirements frequently favor ceramic-metal or dissimilar ceramic component combinations. Joining these different materials by brazing with metal interlayers is a commercially viable technique.

Brazing alloys containing copper, silver and titanium are widely used in metal/ceramic brazing processes. However, Cu(Ag)-Ti/Al₂O₃ brazes often manifest numerous intermetallic compounds. These intermetallic compounds generally deteriorate the mechanical properties of the joint. The objective of this study was to determine the feasibility of joining metals to ceramics using nickel-titanium interlayers in a transient liquid phase brazing process.

Nickel-titanium brazing alloys offer some distinct advantages over copper-titanium alloys. The nickel-titanium phase diagram [1] is shown in Figure 1.1. Nickel-titanium intermetallics do not necessarily deteriorate the properties of the joint. For example, NiTi can exist as a banded martensite shape memory alloy and, as a consequence, provide excellent fracture toughness. Also, the nickel-titanium alloys typically have higher solidus and liquidus lines (at corresponding titanium contents). Although the higher melting

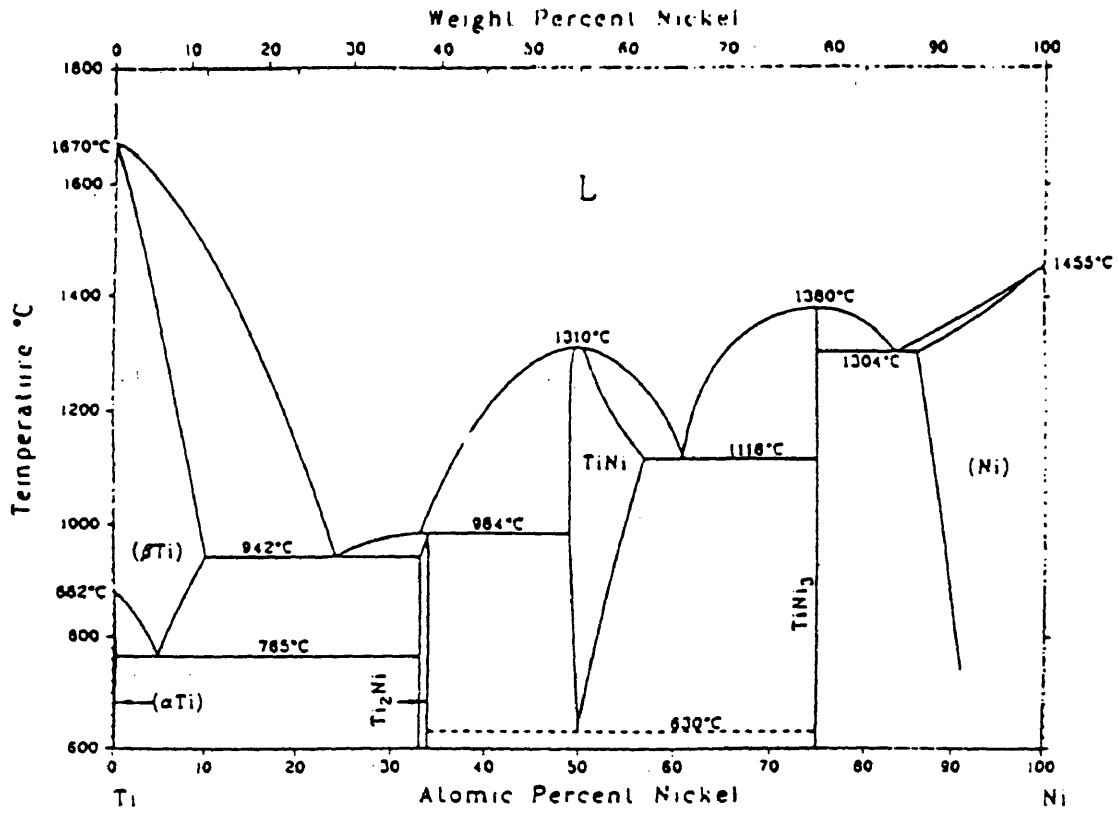


Figure 1.1: Nickel-titanium phase diagram (Massalski [1])

temperatures require higher bonding temperatures, they also allow for higher application temperatures [2].

A. Joining Applications

Current and future applications for joining ceramics to metals and to other ceramics exist in many industries and for a wide range of material combinations. In the electronics industry, applications include multilayer electronic devices that consist of both insulators and electrodes [3], surge arrestors with metal caps brazed to alumina tubes [4], cap and pin type insulators [5], alumina cylinders joined to steel for vacuum tube envelopes [6], and brazed aluminum nitride components [7]. Aerospace applications include silicon nitride turbocharger rotors joined to steel shafts [8]. Other important applications are glass seals [3], high temperature heat exchangers [9], and the cooler brick/casing interface on ceramic high-temperature recuperators [5].

Since the early 1970's, the use of ceramic components in automotive engines has been under intensive development, and currently, trial quantities of ceramic components are being evaluated in a limited number of production automobiles [10]. This has led to new joining applications such as silicon nitride caps on metal push rods [8], partially stabilized zirconia pads joined to nodular iron for rocker arm assemblies [5]; and partially stabilized zirconia, silicon carbide and silicon nitride wear pads joined to nodular iron [6].

Furthermore, the same problems encountered in the aerospace industry when joining gas turbine components such as turbine rotors must be overcome in the automotive industry [5,8].

In addition to conventional joining, the ceramic-metal interface is also important in the processing of metal-matrix composites reinforced with ceramic fibers, whiskers, or particulates (e.g. the casting of aluminum/silicon carbide) [11]; the infiltration of liquid metal into porous ceramics for toughened ceramics [12]; metallizing of hybrid microcircuit substrates [3]; and the containment of liquid metals in ceramic containers during investment casting, where metal-ceramic interactions are undesirable [13].

B. Joining Methods

The most widely used method for joining ceramics is mechanical attachment [4]. Crimping, clamping, shrink fitting and bolting are inexpensive and simple to perform, but these joints lack continuity. Threads and threaded fasteners can be used, but fabricating threads in a ceramic component is difficult and expensive [7]. In addition, it is difficult to fabricate joints which are leaktight or are able to withstand thermal cycling.

Other joining methods include fusion welding, diffusion bonding, brazing, glazing and adhesive bonding [4]. There are very few material combinations which can be fusion welded because of the need for similar melting temperatures and thermal expansion coefficients. Many systems can be adhesively bonded, but the joint performance is

critically dependent on temperature. Diffusion bonding is attractive because lattice distortions can be avoided and no obvious reactions take place. However, this method requires the application of pressure during bonding, which limits the sample geometries that can be joined. Finally, brazing and glazing require a chemical reaction for bonding. In brazing, a metallic coating or a filler metal with an active alloying addition is used to promote wetting of a liquid metal on a ceramic substrate, while in glazing the ceramic surface is oxidized to promote wetting by the molten metal brazes. Unlike diffusion bonding, adhesive bonding, and mechanical attachment, a high temperature thermal cycle is needed for good bonding. In addition, although the initial formation of a reaction layer is beneficial, the thickening of these compounds can cause detrimental stressing of the interface resulting in fracture. The effect of reaction layer thickening and other major factors in ceramic-metal brazing will be discussed in the next section.

C. Important Factors in Brazing

The development of a ceramic-metal brazing process requires the consideration of geometrical, mechanical, and chemical factors [6]. Geometrical factors include the thickness, area, and shape of the interface as well as the relative position of the members. Important mechanical factors are the relative thermal expansions of the filler metal and substrate, the bulk strengths of the filler metal and substrate, and the surface roughness of the substrate. Finally, the important chemical factors are the chemical activities of the

various filler metal components, the tendency to form stable oxides, and the rates of formation and products of any interfacial reaction.

The thermal expansion mismatch between the metal and ceramic is one of the greatest obstacles to successful brazing. There are very few metal/ceramic combinations with similar coefficients of thermal expansion (CTE's) [3]. Upon cooling, the CTE mismatch can lead to large residual stresses. These stresses may cause interfacial cracking and failure [5,11]. The residual stresses can be reduced by using a composite material (e.g. copper-carbon or alumina-tungsten) to change the CTE of the interlayer. More commonly, a very soft, ductile material is used (e.g. silver, copper, aluminum) [12], although most ductile filler metals do not wet most ceramics. Therefore, a small amount of a reactive metal (e.g. titanium or zirconium) is added to the braze filler metal, which promotes wetting by reducing a thin layer of the ceramic [5]. The control of this reaction is important because insufficient reaction leads to incomplete bonding which results in a degradation of joint integrity [13-15]. Excessive reaction and consequent reaction layer thickening can also lead to a degradation of mechanical properties [16,17]. Thus, complete ceramic-metal characterization [3], including the thermodynamics and kinetics of interfacial reactions, the microstructure and composition of the interface reaction, and the structure of the interface at the atomic level is needed to obtain optimal joint properties.

II Literature Review

The literature review covers three major areas related to metal-ceramic bonding. First, wetting and spreading are briefly discussed. General definitions and concepts are presented for both reactive and non-reactive systems. Second, the formation of reaction products within the brazed joint will be explored. Third, current metal-ceramic brazing technology will be reviewed. Reaction product formation, thermodynamics and diffusion theories are presented for metal-ceramic systems with an emphasis on titanium-containing braze alloys on alumina substrates.

A. Wetting and Spreading

The general theories for wetting and spreading are relatively well developed. However, the modeling of experimentally observed spreading behavior for non-reactive as well as reactive systems is difficult and not as well developed.

When a liquid is placed on a solid substrate, several types of wetting and spreading behavior may occur. If the liquid “balls up” or rolls off the surface, it is defined as non-wetting; if the liquid flattens into spherical caps, it is defined as wetting or partially wetting; and if the liquid forms a flattened pancake shape, which continues to spread and cover more of the surface, it is defined as complete wetting or spreading wetting [18-20].

The study of wetting is concerned with the state of the system under a given set of conditions (usually at equilibrium or quasi-equilibrium) while spreading is the study of the changes in wetting behavior with time. However, these definitions are not rigid and considerable overlap of these terms exists. For example, the wetting kinetics of a liquid drop are the same as the spreading kinetics. Therefore, the study of spreading also requires a consideration of the thermodynamics and kinetics of wetting.

1. General Theory

Most studies of wetting are based on the contact angle. The contact angle was first defined empirically by Young in 1805 [18]. He observed that in most cases when a liquid is placed on a solid, the liquid remains as a drop with a definite angle of contact between the liquid and solid phases, shown in Figure 2.1. Setting the forces in the horizontal plane equal to zero at the solid-liquid-vapor triple point results in the Young Equation (or the Young-Dupre Equation) [18,19]:

$$\cos\Theta = \frac{\gamma_{SV} - \gamma_{SL}}{\gamma_{LV}} \quad (1)$$

where Θ = the contact angle

γ_{LV} = the liquid-vapor interfacial energy

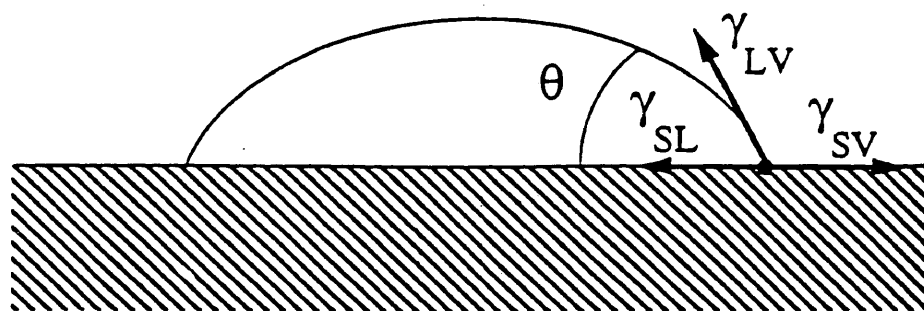


Figure 2.1: Sessile drop schematic diagram illustrating contact angle and relevant interfacial energies

γ_{SV} = the solid-vapor interfacial energy

γ_{SL} = the solid-liquid interfacial energy

In general, a wetting angle greater than 90 degrees is considered non-wetting, and angles between zero degrees and 90 degrees is partially wetting, and an angle of zero degrees is completely wetting. For ceramic-metal brazing, a wetting angle of less than 90 degrees is defined as wetting. A major assumption of this equation is that all of the phases are in thermodynamic equilibrium. While the Young Equation was initially derived based on a surface energy force balance, it can also be derived using a rigorous thermodynamic treatment [21].

2. Measurement of Contact Angle

Several techniques are available for the measurement of contact angles for solid-liquid-vapor systems. These include sessile drop, capillary rise, pendant drop, Wilhelmy slide, the Langmuir-Schaeffer, and the tilting plate methods [20]. Descriptions of these methods are given by Hiemenz [21] and Adamson [22]. Only the sessile drop and capillary rise techniques can be readily adapted to the measurement of non-equilibrium (time-dependent) contact angles and spreading rates.

The most common method for measuring contact angles is the sessile drop method [21,22]. A liquid drop is placed on a flat surface and the contact angle is measured from the solid-liquid interface through the liquid to the liquid-vapor interface (Figure 2.1). The

angle can be measured directly using a microscope or by calculation based on the entire drop profile [21-23]. This method is relatively simple, precise, and reliable but data it yields for ceramic/metal systems is often dictated by additional experimental factors such as the presence and tenacity of the oxide skin covering the drop, or by the time of metal-substrate contact elapsed at the moment of angle measurement [24]. The rate of spreading can also be measured for this geometry by measuring the change in the substrate coverage area, the substrate coverage radius or the contact angle with time.

While the wetting angle is theoretically easy to obtain, external experimental factors can make the actual measurements very difficult. The apparent contact angle has been shown to be strongly dependent upon the measuring device and sample geometry [25]. It is also different for a receding drop versus a spreading drop [21,22,26]. The surface roughness and surface homogeneity also strongly affect the wetting angle. Wenzel's relation is frequently used to correct for the change in contact angle with increases in surface roughness [27]:

$$\cos \Theta = r \cos \Theta^0 \quad (r > 1) \quad (2)$$

Where r = the surface roughness factor
 Θ = the contact angle for the rough surface
 Θ^0 = the contact angle for a smooth surface

The result of this relation is that the contact angle moves away from 90 degrees or a wetting system becomes more wetting ($\Theta \rightarrow 0$ degrees) while a non-wetting system becomes more non-wetting ($\Theta \rightarrow 180$ degrees) with an increase in surface roughness. Usually the value of r is experimentally determined, but attempts have been made to correlate r to the change in surface area for a roughened surface [28]:

$$r = \text{roughness area factor} = \text{true area/nominal area} \quad (3)$$

Other workers [12,26] have correlated the change in contact angle to the average slope of the surface asperities (α_a):

$$\Theta = \Theta_0 + \alpha_a \quad (4)$$

The surface heterogeneities are frequently accounted for using a “rule of mixtures” approach for contact angles [26]:

$$\cos \Theta = f_1 \cos \Theta_1 + f_2 \cos \Theta_2 \quad (5)$$

where f_1 and f_2 are the fractions of the surface having inherent contact angles Θ_1 and Θ_2 .

In terms of the interfacial energies, this formula can also be written as:

$$\gamma_{LV} \cos \Theta = f_1 (\gamma_{S1V} - \gamma_{S1L}) + f_2 (\gamma_{S2V} - \gamma_{S2L}) \quad (6)$$

This approximation generally agrees with experimental results to within ± 15 percent.

3. Non-reactive Systems

In many systems, no reaction takes place when a liquid comes in contact with a solid. Non-reactive spreading and wetting are important in a large number of applications including spreading of molten polymer adhesives, removal of dirt by detergent solutions, dropwise condensation of liquids, displacement of a fluid by another in soils, underground oil reservoirs, packed beds and other porous media, lubrication, soldering, lithographic printing, waterproofing of textiles, cleaning of surface, spray painting, foliage and animal spraying, and electrophotography. Even though a large amount of research has been done in these areas, these processes are not completely understood and many of the existing models are very empirical [20].

4. Reactive Systems

The wetting and spreading behavior of reactive systems is complicated by the interfacial reactions at the solid-liquid interface as well as the reactions at the liquid-vapor interface (e.g. oxidation). Much of the work in ceramic-metal systems has concentrated on predicting the final equilibrium angle based on thermodynamic considerations and on

characterizing the effect of alloying additions and other parameters (i.e. temperature, oxygen partial pressure and surface treatment) on wettability. Very few wetting and spreading kinetics models exist and they are generally empirical in nature.

Aksay et al. [29] identified four different types of reactions which can occur at the solid-liquid interface in a solid-liquid-vapor system:

- 1.) Only the solid is not saturated with some or all components of the liquid.
- 2.) Only the liquid is not saturated with some or all components of the solid.
- 3.) Both phases are unsaturated with respect to the other.
- 4.) A compound forms at the interface.

For reactive metal/ceramic systems, a compound almost always forms at the interface. In nearly all of these systems, an initially non-wetting contact angle ($\Theta > 90$ degrees) decreases with time to a constant wetting angle. A schematic representation of the effect of the formation of a compound at the ceramic metal interface is shown in Figure 2.2. The final contact angle and the time to reach a steady-state angle depend upon the brazing alloy composition and temperature. Examples of wetting systems which exhibit this type of behavior include: eutectic silver-copper alloys with titanium additions on alumina and aluminum nitride [30], aluminum on oxidized silicon carbide and silica [31], aluminum and titanium alloys on silicon nitride [3], aluminum on CVD boron nitride [32], magnesium

alloys on alumina [24], eutectic silver-copper alloys with titanium and zirconium additions on silicon nitride [7], aluminum on silicon carbide [33-36], and copper-titanium and copper aluminum on alumina [37-39]. The time to reach an equilibrium angle can vary from a few seconds to 100 minutes (6000 seconds).

There are several mechanisms by which a reactive metal addition can improve wettability. The contact angle can be lowered by solute metal segregation at the interface or by an interfacial reaction [19]. For example, in the copper-titanium/alumina system, the titanium segregates to the liquid-solid interface while there is both interfacial segregation and the formation of TiO [37]. Solute additions can also increase wettability by lowering the liquid-metal/vapor surface energy. Therefore, the maximum wettability can be achieved by adding two solutes; one that is active at the metal-vapor surface, and one that is active at the metal-ceramic interface.

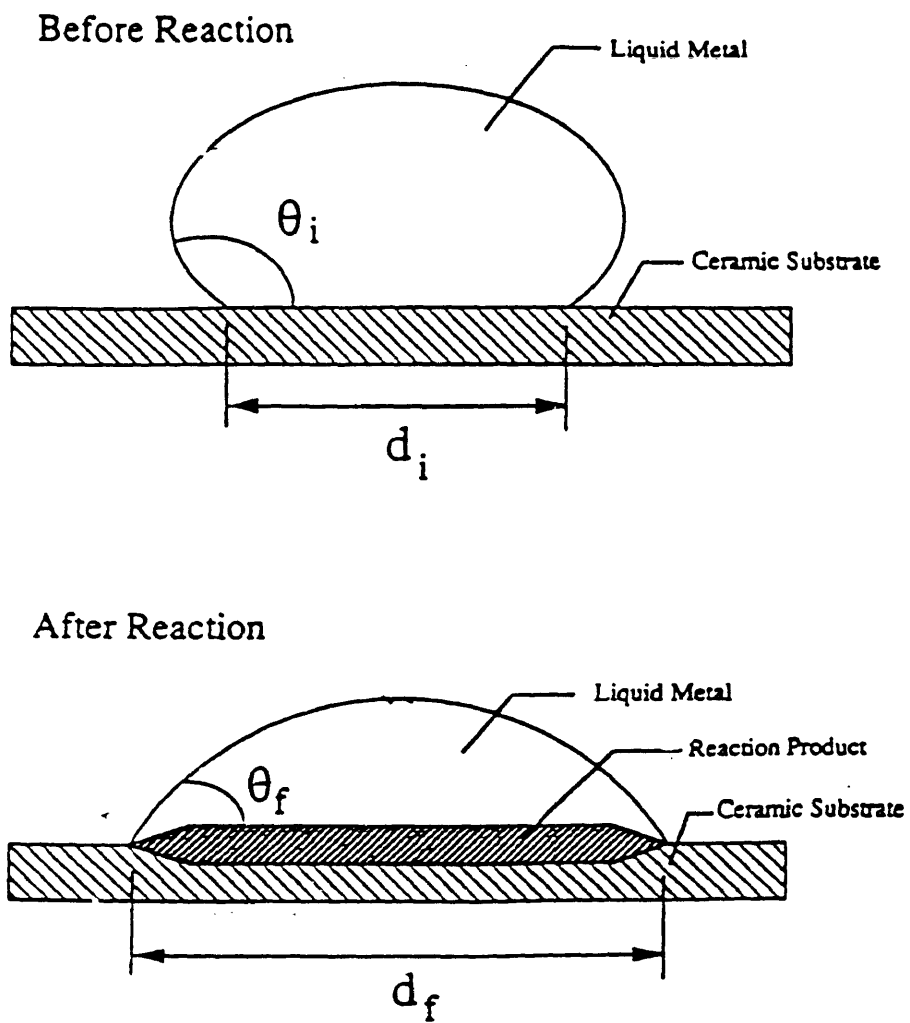


Figure 2.2: Schematic illustration of wetting in a reactive system.

Wettability can be changed by many other techniques besides changing the reactive metal composition or temperature. For many non-oxide ceramics, the oxidation of the solid surface can improve wettability. Examples include aluminum on oxidized silicon nitride [3, 15], and oxidized silicon carbide [31]. Wetting has also been improved by applying a metallic coating before brazing. In the “moly-manganese” process, a molybdenum-manganese coating is sintered on an alumina surface and then brazed [8,40]. Other successful coating applications are titanium, hafnium, tantalum, or zirconium on silicon nitride [41-43].

B. Reaction Layer Formation

Three aspects of reaction layer formation are important in ceramic-metal brazing. The bonding of the metal to the ceramic at the atomic level, the type of products formed, and the rates of reaction product formation all play important roles in determining the appropriate processing parameters for successful ceramic-metal brazing.

1. Ceramic-Metal Bonding

At the interface between a liquid metal and an oxide ceramic, there is a reconstruction of the of the oxide surface with the displacement of the cations to the

interior because of the larger size and higher polarizability of the oxygen anions as compared to the cations [44]. Thus, the adhesion of the metal with the oxides is governed by the interaction of the metal atoms with the oxygen atoms only. A typical oxide is alumina, which is a mixed ionic and electronic conductor at high temperatures [45]. At high temperatures, the metal atoms bond to the alumina. The alumina surface is represented by the cluster $(\text{AlO}_6)^{-9}$. The chemical bond is formed between d-orbital electrons and the non-bonding p-electrons of the oxygen atoms.

Ohuchi [45,46] found that the strong metal-oxygen interaction at the ceramic surface dominated the interfacial bonding for titanium, niobium, copper and nickel with alumina. In the niobium-alumina system, the metal bonded to the ceramic without forming an extended reaction layer while significant electron transfer occurred from titanium to oxygen, for the titanium-alumina system. As a result, aluminum oxygen bonds were reduced to form a lower valence species of aluminum at the interface [46].

Similar work by Nath [47] showed that the bond between (0001) alumina and close-packed transition metal surfaces decreased in strength across the first transition metal series from scandium to copper. This trend as well as the observed decrease in shear strength for the series iron, nickel, copper, and silver on alumina can be explained qualitatively to be caused by the increase in the number of metal-alumina anti-bonding orbitals [48].

Li [38,49] used another approach to explain a linear relationship which exists between the work of adhesion and the electron density. In this model, when a metal approaches an oxide surface and makes atomic contact with it, the thermally created holes in the oxide band can be filled by the free electrons of the metal atoms. The metal atoms which have given their valence electrons to the oxide crystal become cations, and can now interact chemically with the negatively charged oxygen anions present on the oxide surface. These cations then complete the crystalline structure of the material. The intensity of the electron transfer at the interface depends upon the electron density of the metal and the concentration of holes in the oxide valence band. The hole concentration is given by:

$$c = c_0 \exp\left(\frac{-E_g}{2kT}\right) \quad (7)$$

This concept leads to a general rule that the least wetted ceramics tend to be the most ionic and the most chemically stable. For a given oxide, the electron transfer is a function only of the electron density of the metals and would increase with increasing electron density of the metals. For example, in contact with alumina, metals with low electron densities (i.e. copper and silver) have relatively low values for the work of adhesion, while metals with high electron densities (i.e. nickel, platinum and iron) have much higher values for the work of adhesion. This correlation is shown in Figure 2.3.

In addition, oxygen in the melt can aid in Bond formation at a ceramic-metal interface [37]. The oxygen associates with metal atoms in the liquid and forms clusters having a partially ionic character. These clusters can develop coulombic interactions with any ionic or ionocovalent ceramics, and as a consequence, adsorb strongly at metal-oxide interfaces..

2. Possible Products

The interfacial product formed is very important in ceramic-metal brazing for several reasons. For example, if zirconium oxide formation is favored over zirconium nitride formation, the oxide undergoes a transformation to its tetragonal form when the temperature during cooling reaches approximately 1000°C, and the resulting volume change can lead to fracture of the specimen [50]. From the standpoint of wetting and spreading, the reaction products may determine the liquid-solid interfacial energy (if they are at this interface) or they can act as diffusion barriers to the formation of other products (for multilayered products.)

Numerous possible reactions can lower the free energy of a ceramic/metal system, including oxidation, reduction, solution reactions and intermetallic formation [51]:

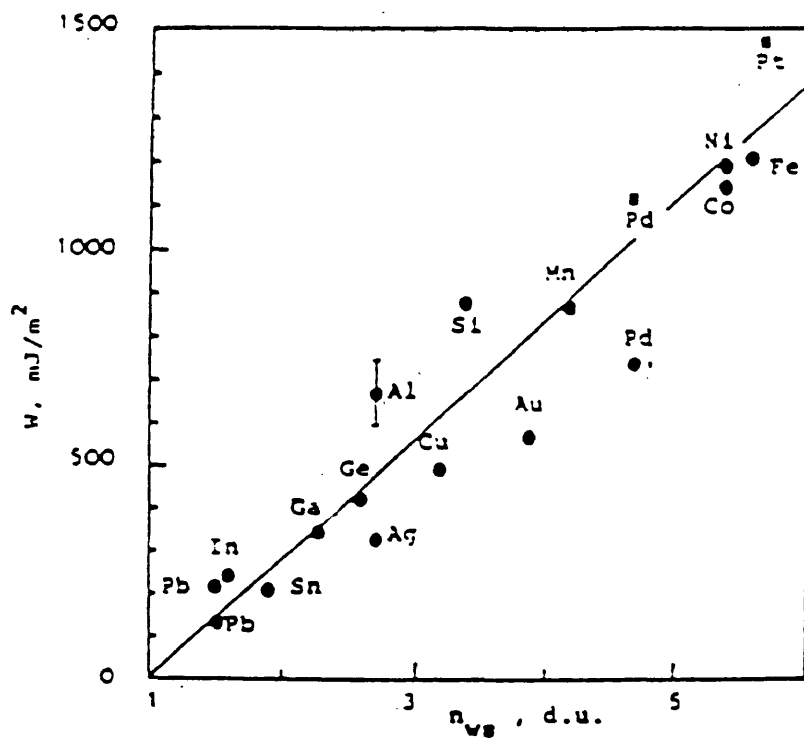
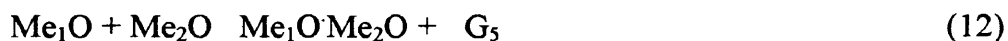
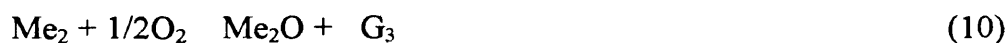


Figure 2.3: Linear relationship between the work of adhesion of different liquid metals on alumina and the electron density, n_{ws} [22].



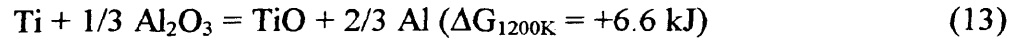
Okamoto [52] ranked the relative stability of oxides, nitrides and carbides at 1200K. The stability for oxides (in decreasing order) is:

Y, Ca, Be, Sr, Mg, Hf, Li, Zr, Al, Ti, Ce, Si, V, Nb, Mn, Cr, Na, Ga, Mo,

Fe, W, In, Ge, Sn, Co, Ni, Cd, Ta, Cu

If one of the metals in the liquid melt forms an oxide more stable than the existing substrate oxide, then a reaction will take place. However the relative stabilities change with temperature (e.g. above 1350 K, titania (TiO) is more stable than alumina). These stability rankings must be used with caution, because the reaction may still occur even if

the bulk thermodynamics predicts a positive free energy change. For example, the following reaction takes place at 1200 K [53]:



Kuranithy [53] attributed the occurrence of this reaction to the tendency of oxygen to dissolve in titanium rather than alumina and its reaction with grain boundary phases.

Other researchers modify the thermodynamic analysis based on surface excess energies.

In a real system, several reaction products can form and the analysis of the reaction layers can become very complicated. For example, in the silver-copper-titanium/silicon carbide system, the following reaction products have all been identified: Ti_5Si_3 , TiC , Ti_3SiC_2 , $\text{Ti}_5\text{Si}_3(\text{C})$, and TiC_{1-x} [54].

The titanium-aluminum-oxygen system is also very complicated. Li et al. [55] compiled data for titanium-alumina diffusion couples from 800 to 1100°C and found the following reported sequences of reaction layers:

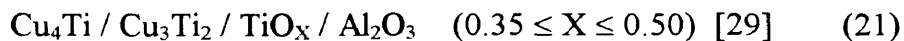
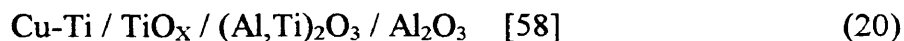




and experimentally obtained the following layer sequence:



where Ti_2O is a saturated solution of oxygen in $\alpha\text{-Ti}$. Other researchers have identified only Ti-Al intermetallics [48, 56], $\text{TiO/Ti}_3\text{Al}$ [52], $\text{TiO/Ti}_2\text{O}_3$ [52], and Ti-Al-O spinels: $(\text{Ti,Al})_2\text{O}_3$ [52,57]. Similar reaction product sequences have been proposed for copper-titanium/alumina systems [18] while other researchers have observed copper-titanium intermetallics in the reaction product sequence including:



Bang and Liu [59] analyzed the products formed in Cu-20w/o Ti/Al₂O₃ brazed joints and found the following reaction product sequence:



The identification of the compounds is frequently complicated by gradients in composition across the interface [57].

Thermodynamic calculations to predict which product will form in the copper-titanium/alumina system have been performed but they are only approximate because they require several estimates of interaction parameters to calculate oxygen activities in the liquid melt [38]. At 1373 K, TiO, Ti₂O₃, or Ti₃O₅ could all be the thermodynamically stable compound for the copper-titanium/alumina system, depending on the oxygen activity.

3. Thickening Kinetics

The thickening of the reaction layer is important because it results in a decrease in the concentration of the active metal in the liquid melt and an increase in the substrate cation from the dissolution of the substrate. The rate of thickening of the reaction product layer is generally diffusion controlled and exhibits parabolic thickening [52,57,60,61]:

$$X = kDt^{1/2}, k = k_0 \exp\left[\frac{-Q}{RT}\right] \quad (23)$$

This relationship was observed for copper-titanium on silicon nitride [60]; titanium on alumina [52]; and titanium, molybdenum, and niobium containing alloys on alumina [57] as well as metal matrix/ceramic fiber systems including titanium/silicon carbide, aluminum/silicon carbide and titanium/borsic [61]. The thickening rates are frequently very rapid [62]. To retard the kinetics of reaction layer growth, a thin film diffusion barrier can be applied or the metal can be alloyed to minimize the thermodynamic driving force [63]. For example, niobium additions have been used to slow down the reaction layer growth of silver-copper-titanium alloys on silicon nitride [62].

Other researchers have found that the thickening of the reaction layer is independent of the contact angle [60]. For copper-titanium on silicon nitride, the reaction layer is discontinuous for very low titanium concentrations and with increasing titanium concentration, the reaction product grows into a thick layer. However, when the concentration is higher than fifteen percent, the thickness decreases considerably, despite a major improvement in wettability. In addition, if a low titanium concentration alloy was heated for long times, the contact angle was reduced very slightly, while the reaction layer grew considerably.

As mentioned above, growth of a reaction layer in metal/ceramic brazing generally shows parabolic behavior. Copper- titanium and copper-zirconium/alumina [64]; copper

niobium, copper-titanium and copper zirconium/silicon nitride [65,66]; titanium and aluminum/alumina [67-69]; and copper titanium/silicon carbide [64] systems all show this type of diffusion controlled reaction layer growth.

An analog to layer growth in ceramic-metal bonds is the growth of an oxide scale on a metal surface. Wagner's theory of oxidation and oxide growth [ZZ] allows an analysis of the growth of an oxide layer and will be presented.

Assuming that ionic transport across the growing oxide layer controls the rate of scaling and that thermodynamic equilibrium is established at each interface, the process can be analyzed as follows. The outward cation flux, $j_{M^{2+}}$, is equal and opposite to the inward flux of cation defects (here taken to be vacancies). This model is shown in Figure 2.4.

Thus

$$j_{M^{2+}} = -j_{V_M} = D_{V_M} \frac{C_{V_M}'' - C_{V_M}'}{x} \quad [24]$$

where x is the oxide thickness, D_{V_M} is the diffusion coefficient for the cation vacancies, and C_{V_M}'' and C_{V_M}' are the vacancy concentrations at the scale-gas and scale-metal interfaces respectively.

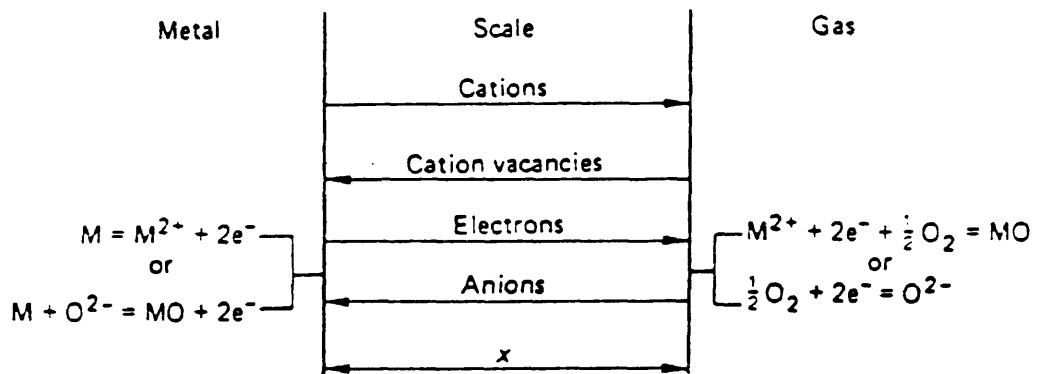


Figure 2.4: Simplified model for diffusion controlled oxidation [66].

Since there is thermodynamic equilibrium at each interface, the value $(C''_{V_M} - C'_{V_M})$ is constant and we have

$$j_{M^{2+}} = -j_{V_M} = D_{V_M} \frac{C''_{V_M} - C'_{V_M}}{x} \quad [25]$$

i.e. $\frac{dx}{dt} = \frac{k'}{x}$ where $k' = D_{V_M} (C''_{V_M} - C'_{V_M})$ [26]

Integrating and noting that $x=0$ at $t=0$

$$x^2 = 2k't \quad [27]$$

which is the common parabolic rate law.

Furthermore, since it has been shown that the cation vacancy concentration is related to the oxygen partial pressure by

$$C_{V_M} = \text{const. } p_{O_2}^{1/n}$$

the variation of the parabolic rate constant with oxygen partial pressure can be predicted

$$k' \propto [(p''_{O_2})^{1/n} - (p'_{O_2})^{1/n}] \quad [28]$$

Since $P'O_2$ is usually negligible compared to $P''O_2$ we have

$$k' \propto (p''_{O_2})^{1/n} \quad [29]$$

Figure 2.5 gives a summary of the conditions, later stated, for which Wagner's theory is valid [ZX]. The following assumptions are made in the development of the theory:

- (1) The oxide layer is a compact, perfectly adherent scale.
- (2) Migration of ions or electrons across the scale is the rate controlling process.
- (3) Thermodynamic equilibrium is established at both the metal-scale and scale-gas interfaces.
- (4) The oxide scale shows only small deviations from stoichiometry.
- (5) Thermodynamic equilibrium is established locally throughout the scale.
- (6) The scale is thick compared with the distances over which space charge effects (electrical double layer) occur.
- (7) Oxygen solubility in the metal may be neglected.

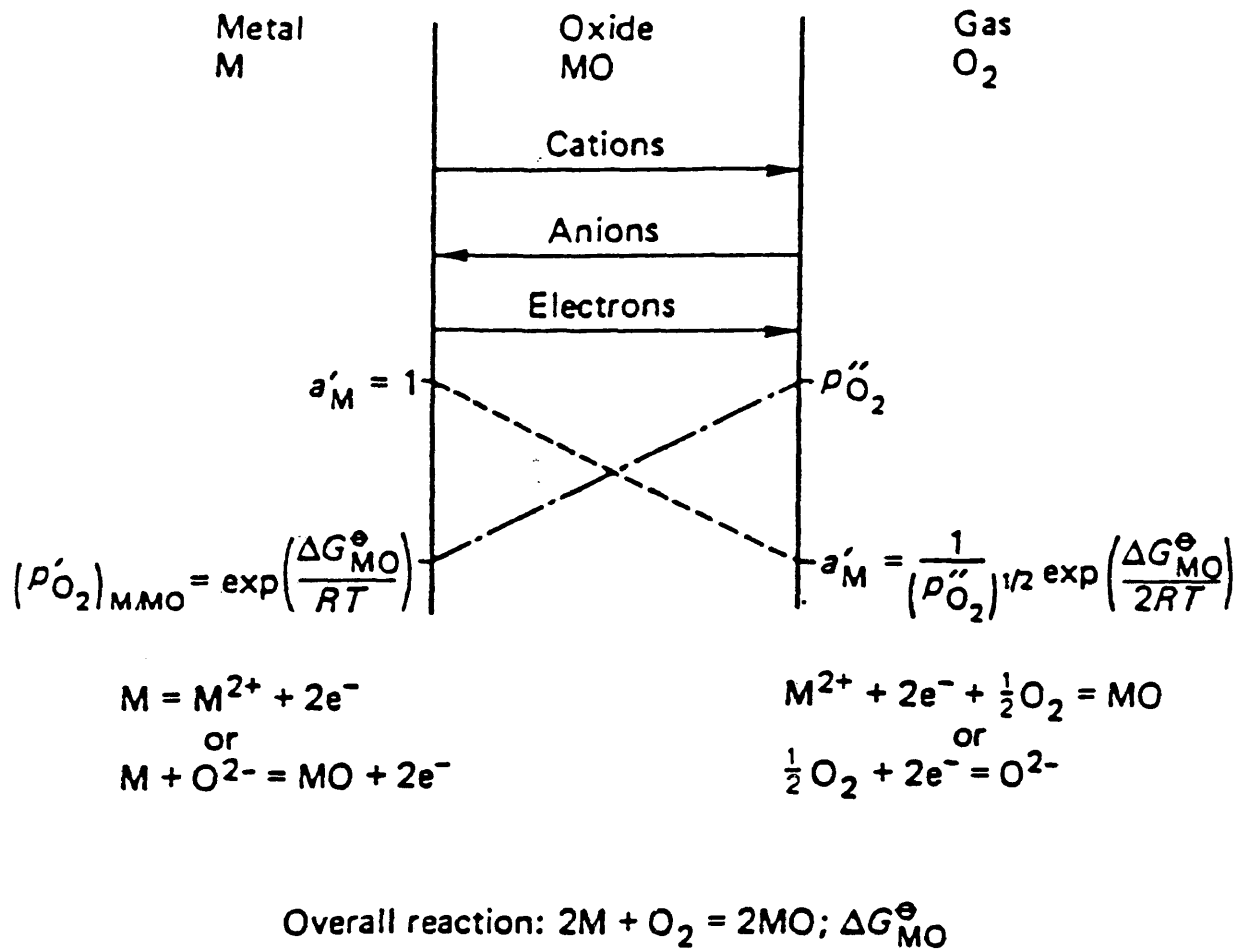


Figure 2.5: Diagram of scale formation according to Wagner's model [66].

Since the thermodynamic equilibrium is assumed to be established at the metal-scale and scale-gas interfaces, it follows that the activity gradients of both metal and non-metal (oxygen, sulfur, etc.) are established across the scale. Consequently, metal ions and oxygen ions will tend to migrate across the scale in opposite directions. Because the ions are charged, this migration will cause an electric field to be set up across the scale resulting in consequent transport of electrons across the scale from metal to atmosphere. The relative migration rates of cations, anions, and electrons are therefore balanced such that no net charge transfer occurs across the oxide layer as a result of ionic migration.

Being charged particles, ions will respond to both chemical and electrical potential gradients which together provide the net driving force for ionic migration.

A particle, I , carrying a charge, Z_i , in a position where the chemical potential gradient is $D\mu_i/Dx$ and the electrical potential gradient is $d\phi/dx$ is acted on by a force given by joules $\text{mol}^{-1} \text{cm}^{-1}$.

$$\text{Or} \quad 1/N_A \left(\frac{\partial \mu_i}{\partial x} + Z_i F \frac{\partial \phi}{\partial x} \right) \text{ joules particle}^{-1} \text{cm}^{-1} \quad [30]$$

where N_A is Avogadro's number and F is the Faraday constant in coulomb mol^{-1} .

Moving through an ionic lattice under a constant force, an ion rapidly assumes a constant velocity known as the terminal drift velocity. The value of the terminal drift

velocity when the ion is acted on by unit force is known as the mobility, B_i , of the species. Therefore, the flux of I, acted on by the force given in equation 30, is

$$j_i = c_i B_i / N_A \left(\frac{\partial \mu_i}{\partial x} + Z_i F \frac{\partial \phi}{\partial x} \right) \text{ particles cm}^{-2} \text{ s}^{-1} \quad [31]$$

where c_i is the concentration of i in particles cm^{-3} .

Alternatively

$$j_i = -\frac{c_i B_i}{N_A} \left(\frac{\partial \mu_i}{\partial x} + Z_i F \frac{\partial \phi}{\partial x} \right) \text{ mols cm}^{-2} \text{ s}^{-1} \quad [32]$$

The mobility and partial conductivity of species i are related by

$$c_i B_i = \frac{\sigma_i}{Z_i^2 e^2} \quad [33]$$

where σ_i is the partial electrical conductivity of I and e is the electronic charge, thus

$$j_i = -\frac{\sigma_i}{Z_i^2 F^2} \left(\frac{\partial \mu_i}{\partial x} + Z_i F \frac{\partial \phi}{\partial x} \right) \quad [34]$$

Equation 34 can be used to describe the flux of cations, anions, or electrons through the oxide layer. Due to their different mobilities, different species would tend to move at different rates, however, this would set up electric fields tending to oppose this independence. In fact, the three species migrate at rates that are defined by the necessity on maintaining electroneutrality throughout the scale, i.e. such that there is no net charge across the oxide scale. This condition is usually achieved due to the very high mobility of electrons or electronic defects.

The original treatment by Wagner involved cations, anions, and electrons. However, the majority of oxides and sulfides show high electronic mobility and the mobilities of the cation and anion species usually differ by several orders of magnitude. It is, therefore, possible to ignore the migration of the slower moving ionic species and thus simplify the treatment somewhat.

The most frequently met case involves oxides and sulfides in which cations and electrons are the mobile species. Writing Z_c and Z_e for the charges on the cations and electrons respectively, and using equation 34, we have for the respective fluxes

$$j_i = -\frac{\sigma_c}{Z_c^2 F^2} \left(\frac{\partial \mu_c}{\partial x} + Z_c F \frac{\partial \phi}{\partial x} \right) \quad [35]$$

and

$$j_i = -\frac{\sigma_e}{Z_e^2 F^2} \left(\frac{\partial \mu_e}{\partial x} + Z_{ei} F \frac{\partial \phi}{\partial x} \right) \quad [36]$$

The condition for electrical neutrality is

$$Z_c j_c + Z_e j_e = 0 \quad [37]$$

and, using equations 35, 36, and 37, it is now possible to eliminate $\partial \phi / \partial x$ as

$$\frac{\partial \phi}{\partial x} = -\frac{1}{F(\sigma_c + \sigma_e)} \left[\frac{\sigma_c}{Z_c} \frac{\partial \mu_c}{\partial x} + \frac{\sigma_e}{Z_e} \frac{\partial \mu_e}{\partial x} \right] \quad [38]$$

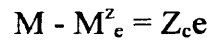
Substituting 38 in equation 35 we have for the flux of cations

$$j_c = -\frac{\sigma_c \sigma_e}{Z_c^2 F^2 (\sigma_c + \sigma_e)} \left[\frac{\partial \mu_c}{\partial x} - \frac{Z_e}{Z_c} \frac{\partial \mu_e}{\partial x} \right] \quad [39]$$

Since the electronic charge $Z_e = -1$, equation 39 becomes

$$j_c = -\frac{\sigma_c \sigma_e}{Z_c^2 F^2 (\sigma_c + \sigma_e)} \left[\frac{\partial \mu_c}{\partial x} + Z_c \frac{\partial \mu_e}{\partial x} \right] \quad [40]$$

The ionization of a metal M is represented by



and it follows that, at equilibrium

$$\mu_M = \mu_c + Z_c \mu_e \quad [41]$$

Therefore, from equations 40 and 41

$$j_c = -\frac{\sigma_c \sigma_e}{Z_c^2 F^2 (\sigma_c + \sigma_e)} \frac{\partial \mu_M}{\partial x} \quad [42]$$

Equation 42 is the expression for the cationic flux at any place in the scale, where σ_c , σ_e and $\partial \mu_M / \partial x$ are the instantaneous values at that place. Since all of these values may change with the position in the scale, it is necessary to integrate equation 42 in order to define j_c in terms of the scale thickness, x , and the measurable metal chemical potentials at the metal-scale, u'_M , and scale-gas, u''_M , interfaces, i.e.

$$j_c = -\frac{1}{Z_c^2 F^2 x} \int_{\mu_M}^{\mu_M'} \frac{\sigma_c \sigma_e}{\sigma_c + \sigma_e} d\mu_M$$

or

$$j_c = \frac{1}{Z_c^2 F^2 x} \int_{\mu_M}^{\mu_M'} \frac{\sigma_c \sigma_e}{\sigma_c + \sigma_e} d\mu_M \quad \text{mol cm}^{-2} \text{s}^{-1} \quad [43]$$

If the concentration of metal in the oxide scale is $C_M \text{ mol cm}^{-3}$ then the flux may also be expressed by

$$j_c = C_M \frac{dx}{dt} \quad [44]$$

where x is the oxide scale thickness.

The parabolic rate law is usually expressed as

$$\frac{dx}{dt} = \frac{k'}{x} \quad [45]$$

where k' is the parabolic rate constant is $\text{cm}^2 \text{s}^{-1}$.

Comparing equations 43, 44, and 45, the parabolic rate constant is expressed by

$$k' = \frac{1}{Z_c^2 F^2 x C_M} \int_{\mu'_M}^{\mu''_M} \frac{\sigma_c \sigma_e}{\sigma_c + \sigma_e} d\mu_M \quad [46]$$

A similar treatment for the case where anions are more mobile than cations, i.e. the migration of cations may be neglected, yields

$$k' = \frac{1}{Z_c^2 F^2 x C_X} \int_{\mu'_X}^{\mu''_X} \frac{\sigma_a \sigma_e}{\sigma_a + \sigma_e} d\mu_X \quad [47]$$

where σ_a is the partial electrical conductivity of the anions and X is the non-metal, oxygen or sulfur.

In general, it is found that the transport number of electrons, or electronic defects, is close to unity, compared with which the transport numbers of cations or anions are negligibly small. In these cases, equations 46 and 47 reduce to

$$k' = \frac{1}{Z_c^2 F^2 x C_M} \int_{\mu'_M}^{\mu''_M} \sigma_c d\mu_M \quad \text{cm}^2 \text{s}^{-1} \quad [48]$$

and

$$k' = \frac{1}{Z_c^2 F^2 x C_x} \int_{\mu_x}^{\mu_x} \sigma_a d\mu_x \quad \text{cm}^2 \text{s}^{-1} \quad [49]$$

respectively.

The mobility, B_i , and diffusion coefficient, D_i , of a species are related by the Nernst-Einstein equation

$$D_i = B_i k T \quad [50]$$

where k is Boltzmann's constant and T is absolute temperature. Introducing equation 33

$$c_i B_i = \frac{\sigma}{Z_i^2 e^2} \quad [33]$$

we have

$$D_i = \frac{kT\sigma_i}{Z_i^2 e^2 c_i} \quad [51]$$

where c_i is the concentration in particles cm^{-3} . Thus

$$D_i = \frac{RT\sigma_i}{Z_i^2 F^2 C_i} \quad [52]$$

where C_i is the concentration in mols cm^{-3} .

Consequently, using equations 48, 50, and 51, we have

$$k' = \frac{1}{RT} \int_{\mu_M}^{\mu_M'} D_M d\mu_M \quad \text{cm}^2 \text{s}^{-1} \quad [53]$$

and

$$k' = \frac{1}{RT} \int_{\mu_X}^{\mu_X'} D_X d\mu_X \quad \text{cm}^2 \text{s}^{-1} \quad [54]$$

for the parabolic rate constant, where D_M and D_X are the diffusion coefficients for metal, M, and non-metal, X, through the scale respectively.

Equations 53 and 54 are written in terms of variables that can be measured relatively easily, although it is assumed that the diffusion coefficient is a function of the chemical potential of the species involved.

Thus, in order to be able to calculate values of the parabolic rate constant, the relevant diffusion coefficient must be known as a function of the chemical potential of the mobile species. Such data are frequently not available or are incomplete. Furthermore, it is usually easier to measure the parabolic rate constant directly than to carry out experiments to measure the diffusion data. Thus, the real value of Wagner's analysis lies in providing a complete mechanistic understanding of the process of high temperature oxidation under the conditions set out.

In the above treatment the parabolic rate constant is derived for the units relating to measurements of the oxide thickness as the reaction parameter. As mentioned before, there are several methods of following the reaction, depending on choice of reaction parameter, each of which produces its own particular parabolic rate constant, as shown below using Wagner's notation for the various parabolic rate constants [ZY].

(a) *Measurement of scale thickness (x)*

$$\frac{dx}{dt} = \frac{k'}{x} \quad \text{i.e.} \quad x^2 = 2k' t \quad [55]$$

k' is the "practical tarnishing constant" or "scaling constant" and has units of cm^2s^{-1}

(b) *Measurement of the mass increase of the specimen (m)*

The parabolic rate constant k'' is defined by

$$\left(\frac{m}{A}\right)^2 = k'' t \quad [56]$$

where A is the area over which the reaction occurs

k'' is also referred to as the "practical tarnishing" or "scaling constant" and has units of $\text{g}^2\text{cm}^{-4}\text{s}^{-1}$.

(c) *Measurement of metal surface displacement (l)*

Measuring the thickness of metal consumed leads to the relationship defining k_c

$$l^2 = 2 k_c t \quad [57]$$

k_c is called the "corrosion constant" and has units of cm^2s^{-1} .

(d) *Rate of growth of scale of unit thickness*

The relevant rate constant is defined as the rate of growth over unit area in equivalents per second of a scale of unit thickness i.e.

$$k = \frac{x}{A} \frac{dn}{dt} \quad [58]$$

where n is the number of equivalents in the oxide layer of thickness x.

k is called the “theoretical tarnishing constant” and has units of equivalents $\text{cm}^{-1}\text{s}^{-1}$. This is sometimes called the rational rate constant and denoted k_r .

It is easy to see that having so many different ways of expressing parabolic rate constants, and so many different symbols, produces a situation ripe for confusion. Consequently, it is necessary to check the definition of a rate constant very carefully when evaluating quantitative data.

It is easy to calculate the value of any rate constant from any other since they all represent the same process.

This type of analysis has been used to determine the activation energies for reaction layer growth in several metal/ceramic systems. In Si_3N_4 brazed with copper titanium, the reaction layer consisted of TiN. An activation energy of 237 kJmol^{-1} was measured for this process [68]. In brazed joints of alumina with titanium, an activation energy of 142 kJmol^{-1} was reported [71]. Baldwin et al. [69] reported an activation energy of 309 kJ mol^{-1} for the growth of a CuAlO_2 reaction layer on alumina.

C. Current Technology in Metal/Ceramic Brazing

1. General Metal/Ceramic Brazing

Recent research into metal/ceramic brazing has been aimed at developing brazing processes and interlayer materials that give improved properties. Properties such as bond

strength, especially at high temperatures, and corrosion resistance are particularly important. [72].

There are still several problems to be solved for the perfect bonding. The thermal expansion mismatch between ceramics and metals is one of them. When the joints are bonded at elevated temperatures, thermal expansion mismatch produces a large stress concentration in the joints. This stress sometimes brings about fatal damage in the joints without any applied forces. Hence compensation for this mismatch is needed to get high strength joints.

Several methods, some using interlayers, have been developed for this purpose. Nichols and Crispin [73] developed a soft metal method using aluminum as an interlayer for the bonding of alumina to an austenitic stainless steel. They achieved joints with a tensile strength of 70 MPa. Suganuma et al. used an aluminum/Invar alloy interlayer for the bonding of silicon nitride to a ferritic steel [72,75]. The strength of the joint reached a bending strength of 170 MPa. However, there are limits to the serviceable temperature and to the strength of the joints because of using a ductile, low melting point metal such as aluminum.

H. Lee and J. Lee [77] studied the bond strength in brazing of silicon carbide by several copper-based interlayer materials. Copper-titanium is a commonly used brazing alloy for this application, but it has several disadvantages which have led to development of several other alloys. Titanium is easily oxidized in the atmosphere owing to its high

reactivity with oxygen. The high reactivity of titanium makes control of the alloy composition difficult in the production of brazing alloys. Brazing alloys in the form of paste can deteriorate in long term storage because of the high reactivity of fine powders composing the paste. This has led to the development of less reactive brazing alloys that easily wet ceramics and have good bond strength.

In these less reactive brazing alloys vanadium, niobium and chromium were chosen as substitutes for titanium. Other possible transition elements, such as zirconium and hafnium are too reactive, while tantalum, molybdenum and tungsten have little reactivity with silicon carbide.

Four point bend strengths for the resulting joints were measured for each brazing alloy composition. Figure 2.6 shows the bend strength for each composition tested. Samples brazed with copper-chromium interlayers broke during cooling from the brazing temperature. Good results were obtained from the copper-2 at % niobium samples, with a strength of 154 MPa, while specimens brazed with 5 at % titanium, 5 at % vanadium, and 5 at % niobium all had similar bend strengths of about 90 MPa [77].

2. Transient Liquid Phase Brazing

Transient liquid phase (TLP) bonding has been employed in a range of applications, since it produces joints that have microstructural and hence mechanical

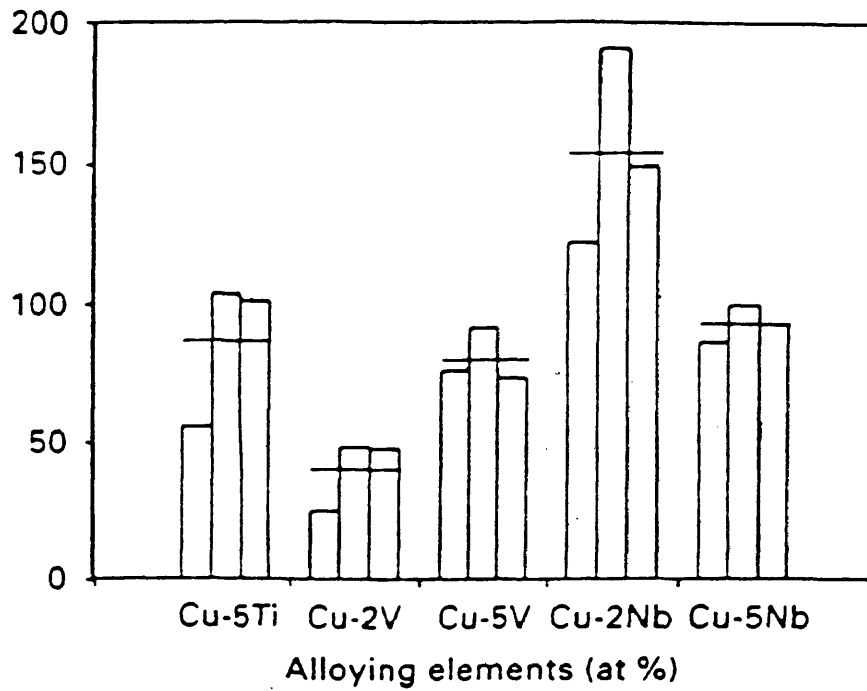


Figure 2.6: Four-point bend test results of the brazed joints by Cu-X alloys [77].

properties similar to those of the base material. Transient liquid phase bonding has the following advantages [82]:

1. Joint formation depends on an isothermal, relatively low temperature bonding mechanism.
2. No interface remains after the TLP bonding operation.
3. Since the joining technique depends on capillary filling, the joint preparation before TLP bonding is relatively simple.
4. In contrast to diffusion bonding, the joining process is highly tolerant to the presence of a faying surface oxide layer. For this reason, and because of the absence of thermal stresses, TLP bonding is ideal when joining intermetallic base materials which have stable oxide surface films, are highly sensitive to microstructural changes, and have poor low temperature ductility.
5. The bonding process is ideal when joining base materials which are inherently susceptible to hot cracking or post-weld heat treatment cracking problems.
6. The bonding process is ideally suited for the fabrication of large and complex shaped components [82].

Transient liquid phase bonding has been used when joining nickel based and iron based superalloy materials [81,82], titanium alloys [83], stainless steel [84], silicon nitride to superalloys[73], and silicon nitride to titanium alloys [85].

TLP bonding can be characterized by separating the process into four discrete stages. Figure 2.7 shows a schematic of the different stages during the TLP brazing cycle. These stages are further explained below.

Stage 1: This is the heating stage, where the component is heated from room temperature to the filler metal melting temperature (from point 0 to point a in Figure 2.8). During heating, interdiffusion occurs between the filler metal and base material, changing the composition at the base material/filler metal interface.

Stage 2: This is the dissolution stage (from point a to point b and then to point c in Figure 2.8), when the base metal dissolves into the liquid and hence the width of the liquid zone increases. This stage can be subdivided as follows.

Stage 2-1: In this stage, the temperature increases from the melting point to the bonding temperature (point a to point b).

Stage 2-2: This is when isothermal dissolution occurs at the bonding temperature (point b to point c). At the end of stage 2, the liquid zone has reached its maximum width.

Stage 3: This is the isothermal solidification stage, where the liquid zone solidifies as a result of solute diffusion into the base metal at the bonding temperature (from point c to point d). The width of the liquid zone decreases continuously until the joint completely solidifies. The solute

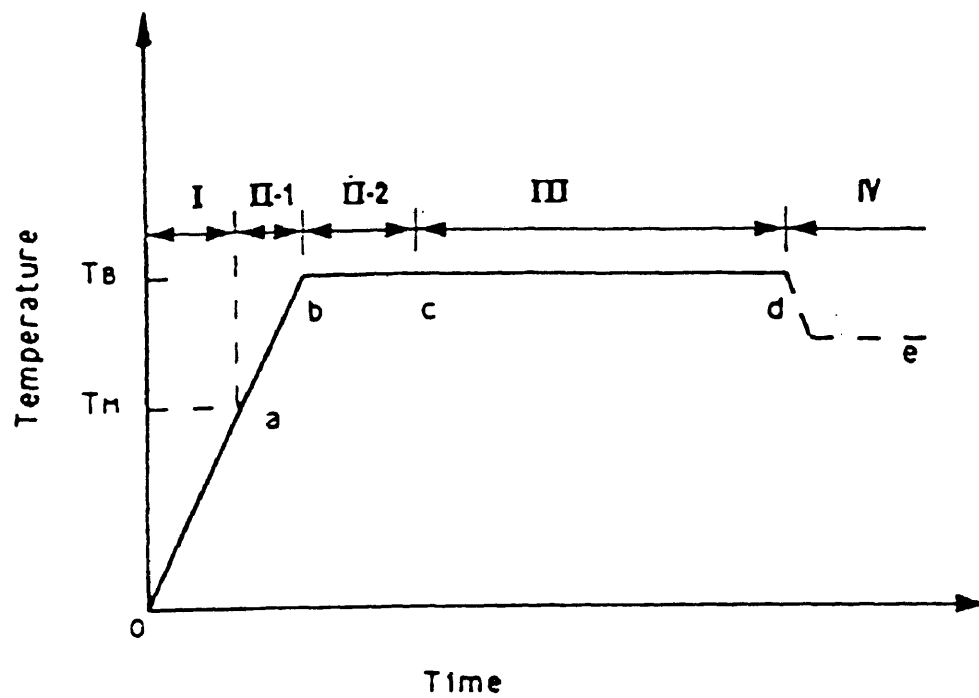


Figure 2.7: Schematic showing different stages during TLP bonding, where T_B is the bonding temperature and T_M is the melting point of the filler metal [82].

distribution in the liquid is uniform during almost all of the isothermal solidification stage. The isothermal solidification stage is generally considered the most important since the completion time required for the TLP brazing process is largely determined by the time required for the completion of solidification.

Stage 4: This is the homogenization stage where solid state solute redistribution occurs (from point d to point e) [82].

Analytical modeling of TLP brazing depends on classical solutions for Fick's diffusion equations. Two cases will be presented for the following discussion.

The first case occurs when the surface of a semi-infinite specimen with an initial solute concentration C_M is maintained at composition C_0 for all $t > 0$ values, i.e.:

$$C(y,0) = C_M \quad (59)$$

$$C(0,t) = C_0 \quad (60)$$

where t is time and y is the distance from the surface, and the solute concentration in the specimen is:

$$C(y,t) = C_0 + (C_M - C_0) \operatorname{erf} \left(\frac{y}{(4Dt)^{1/2}} \right) \quad (61)$$

where D is the solute diffusion coefficient. The rate at which the diffusing species enters the specimen is given by the relation

$$\left(D \frac{\partial C}{\partial y} \right)_{y=0} = \frac{D(C_M - C_0)}{(\pi Dt)^{1/2}} \quad (62)$$

The total amount M_t of diffusing substance which has entered the medium at time t is found by integrating the above equation with respect to t

$$M_t = 2(C_0 - C_M) \left(\frac{Dt}{\pi} \right)^{1/2} \quad (63)$$

The second case is when the initial thickness ($2h$) of the source of the diffusing species (c_0) is of the order of the diffusion distance $(Dt)^{1/2}$, i.e.

$$C(y,0) = C_0 \quad h \geq y \geq 0 \quad (64)$$

$$C(y,0) = C_M \quad y > h \quad (65)$$

where C_M is the initial concentration of the diffusing species in the specimen. The solute concentration is given by the relation [82]

$$C(y,t) = C_M + 1/2(C_0 - C_M) * \left\{ \operatorname{erf}\left[\frac{y+h}{(4Dt)^{1/2}}\right] - \operatorname{erf}\left[\frac{y-h}{(4Dt)^{1/2}}\right] \right\} \quad (66)$$

III Experimental Procedure

Two types of experimental testing incorporating nickel-alumina bonding were undertaken. First, a procedure for the manufacture of the testing samples was developed. The samples were then subjected to two types of experimentation. The first testing was mechanical testing, performed through a four-point bending setup. The second testing was an electron microscope analysis to obtain compositional profiles across the nickel-alumina interface. This information can be used in a kinetic analysis of the bonding process.

A. Materials Used

Alumina was chosen as the ceramic material in this study because relatively high purity polycrystalline material is easy to obtain and relatively inexpensive. For this investigation 0.5-in-dia AD-998 α -alumina rod was obtained from Coors Ceramics Company. Alumina tubes (0.75-in-OD; 0.56-in-ID) were also obtained from Coors. 99.5 percent pure nickel rods 0.5-in-dia. 99.7 percent pure nickel powder (-50+100 mesh) and 99.5 percent pure titanium powder (-100 mesh) was obtained from Alpha Aesar Company. Alumina boats from Coors Ceramics Company were used as vessels to contain any spills

while in the vacuum furnace, as well as to hold titanium sponge used as an oxygen getter during the brazing.

B. Creation of Samples

The samples were created by creating a sandwich configuration of titanium-nickel powder / pure nickel / titanium-nickel powder between two alumina rods. A schematic diagram of this configuration is shown in Fig 3.1. Both the composition of the powder layers and the thickness of the pure nickel disk in the center were controlled. The powders were mixed in two compositions: 30 weight percent nickel, 70 weight percent titanium; and 40% weight percent nickel, 60 weight percent titanium. These compositions were chosen as optimal for transient liquid phase brazing. The pure nickel disk was formed by slicing the nickel rod with a low-speed diamond saw. The resulting disks were then ground to a 1mm thickness.

The samples were then brazed at temperatures of 1100, 1150, 1200, and 1250°C in a vacuum furnace. Figure 3.2 shows a graphic representation of the thermal cycle that was followed. The samples were held isothermally at 200°C to evaporate any moisture that was present, followed by a heating to 900°C and an isothermal period to burn off any binder used in the ceramic manufacturing. Following this practice, the sample were heated to the brazing temperature and held for a specified time. For each brazing temperature, the samples were held at temperature for 0, 10, and 30 minutes. Samples

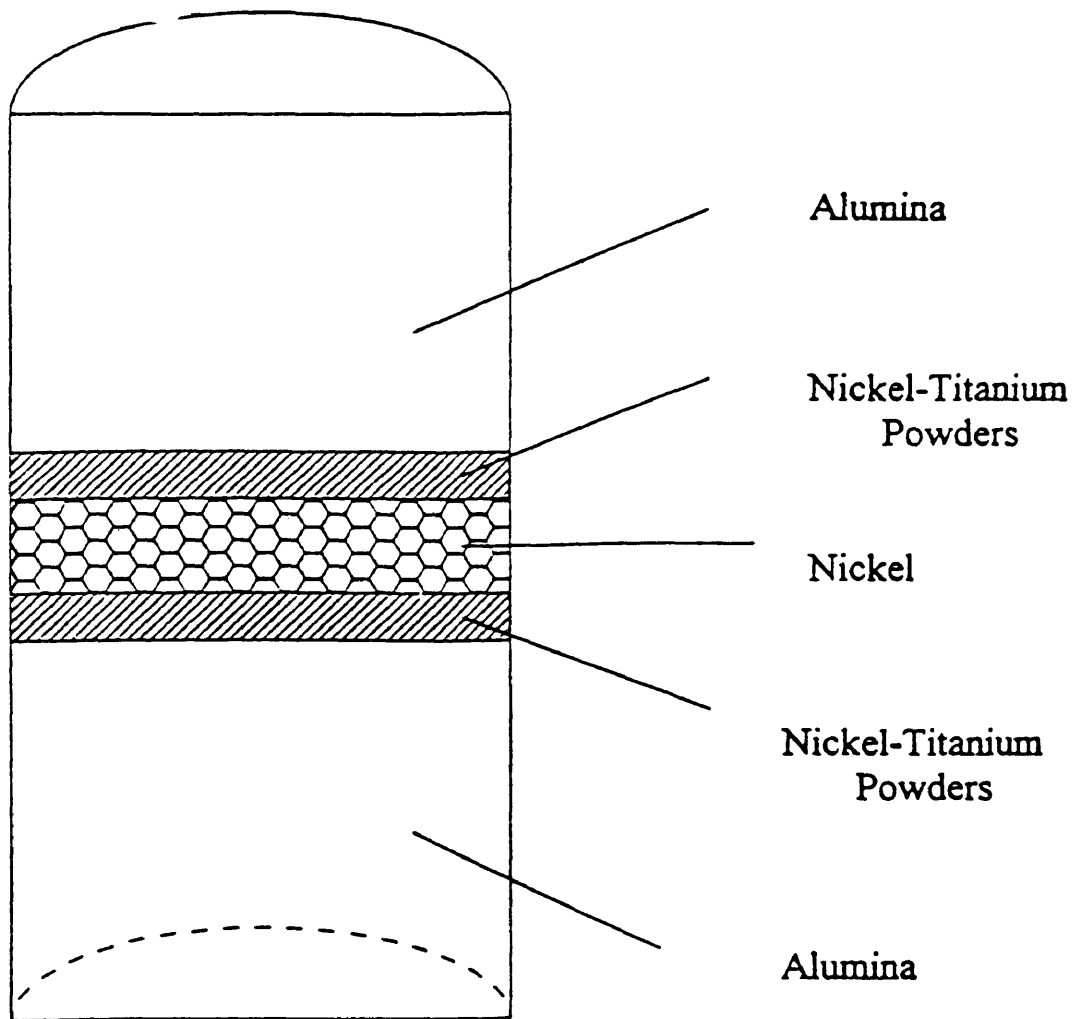


Figure 3.1: Sample configuration used in TLP brazing experiments with nickel-titanium interlayers.

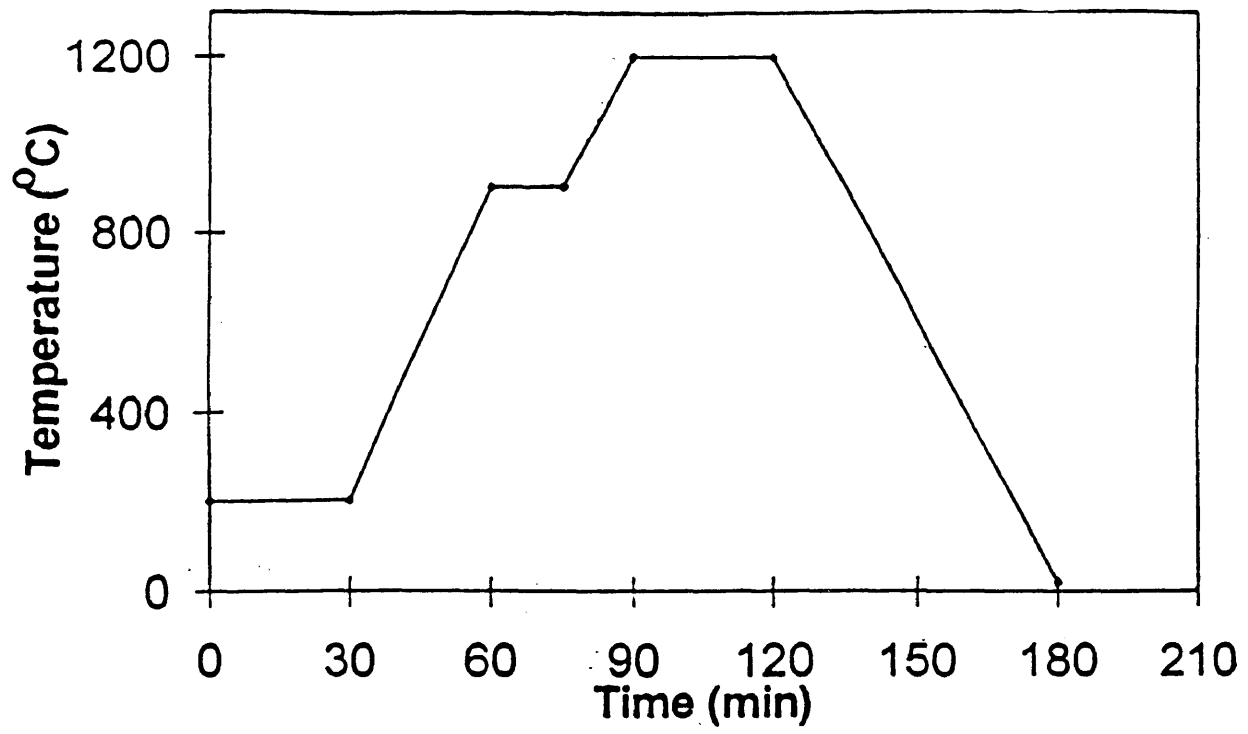


Figure 3.2: Thermal cycle used in TLP brazing of alumina to nickel.

were also held for 150 and 300 minutes at 1150 and 1200°C. Titanium sponge was used as an oxygen getter in the furnace while the brazing occurred and a slight (approx. 1 psi) overpressure of pure argon gas was maintained to insure against oxygen contamination of the furnace atmosphere. Once the brazed samples were complete, they were divided into mechanical testing samples and electron microscopy samples. Samples that were created by brazing at 1150 and 1200°C for 150 and 300 minutes were used only for mechanical testing. Samples that were created at 1250°C for all hold times were used only for electron microscope analysis.

C. Méchanical Testing

The samples that were created for mechanical testing were machined to form rectangular bars from the round samples. This practice was done by first cutting the sample in half lengthwise with a high speed diamond saw. The two halves were then ground into bars with a 64 micron alumina grinding wheel in the Geology department. Figure 3.3 shows a representative bar with relevant dimensions. These bars were then tested on an Instron mechanical testing frame with a four point bending fixture. Once the samples had failed, the fracture surfaces were analyzed in the SEM to determine where in the interface the failure occurred.

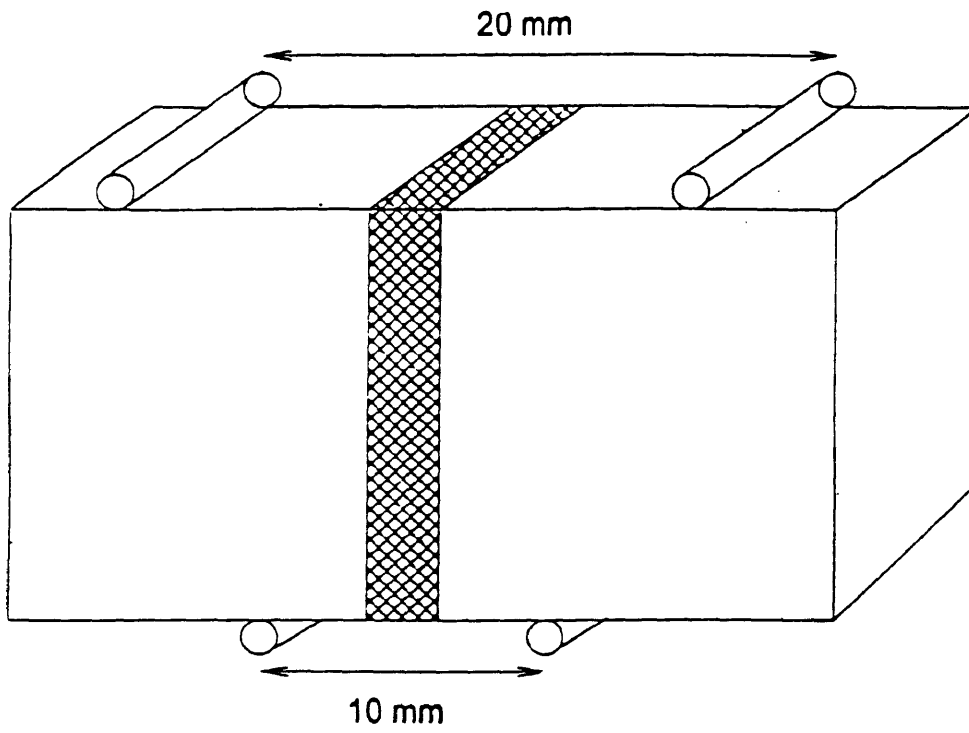


Figure 3.3: Four-point bend sample showing relevant dimensions.

D. Scanning Electron Microscope Analysis

As mentioned above, half of the samples prepared were used for analysis in a scanning electron microscope (SEM). These samples were cut in half to create a flat surface across the metal-ceramic interface. This surface was then ground with the 64 micron alumina grinding wheel in the Geology Department. The surface was then polished with six micron and one micron diamond polishing wheels. The surface was further prepared by coating the polished surface with carbon, to give a conductive surface. The samples were placed in a Jeol JXA840 SEM for analysis. Using electron dispersive spectroscopy (EDS), the chemical composition of any point on the surface can be determined. This technique was applied to these samples by scanning points on the sample ten microns apart on a line perpendicular to the metal ceramic interface. Figure 3.4 shows a micrograph of one of the interfaces, along with the line of the compositional point scans.

Using the data generated by the SEM, compositional profiles for each sample were created. These profiles were then used to determine thicknesses of the various layers that were formed during the brazing process.

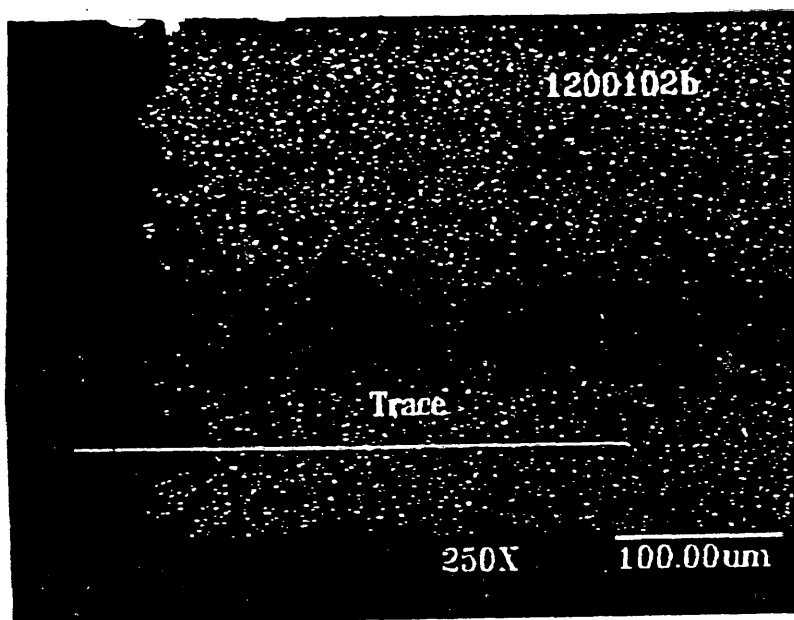


Figure 3.4: Micrograph of nickel-alumina interface and interlayer region, showing trace of SEM scan.

IV Results

A. Mechanical Testing

As mentioned above, the samples were tested in four point bending. All samples prepared at 1100C showed zero bond strength for all times at temperature. Processing at 1150C shows increasing bond strength with time up to a maximum at approximately thirty minutes, then decreasing strength for times greater than thirty minutes. Figure 4.1 shows the strength of the 40 weight percent Ni-60 weight percent Ti samples at 1150C and Figure 4.2 shows the strength of the 30 weight percent Ni-70 weight percent Ti samples at 1150C as a function of time at temperature. At 1200C the maximum bond strength was reached quite rapidly, within ten minutes. After about ten minutes, the strength decreases as the time at temperature increases. Figure 4.3 shows the strength of the 40 weight percent Ni-60 weight percent Ti samples at 1200C and Figure 4.4 shows the strength of the 30 weight percent Ni-70 weight percent Ti samples at 1200C as a function of time at temperature.

Using the volume fraction of each phase, a meaningful correlation between microstructure and strength can be shown. Figure 4.5 shows the strength measured for each sample with a 30 weight percent Ni-70 weight percent Ti interlayer plotted against the ratio of volume fraction of Ni_3Ti divided by the volume fraction of NiTi. Figure 4.6

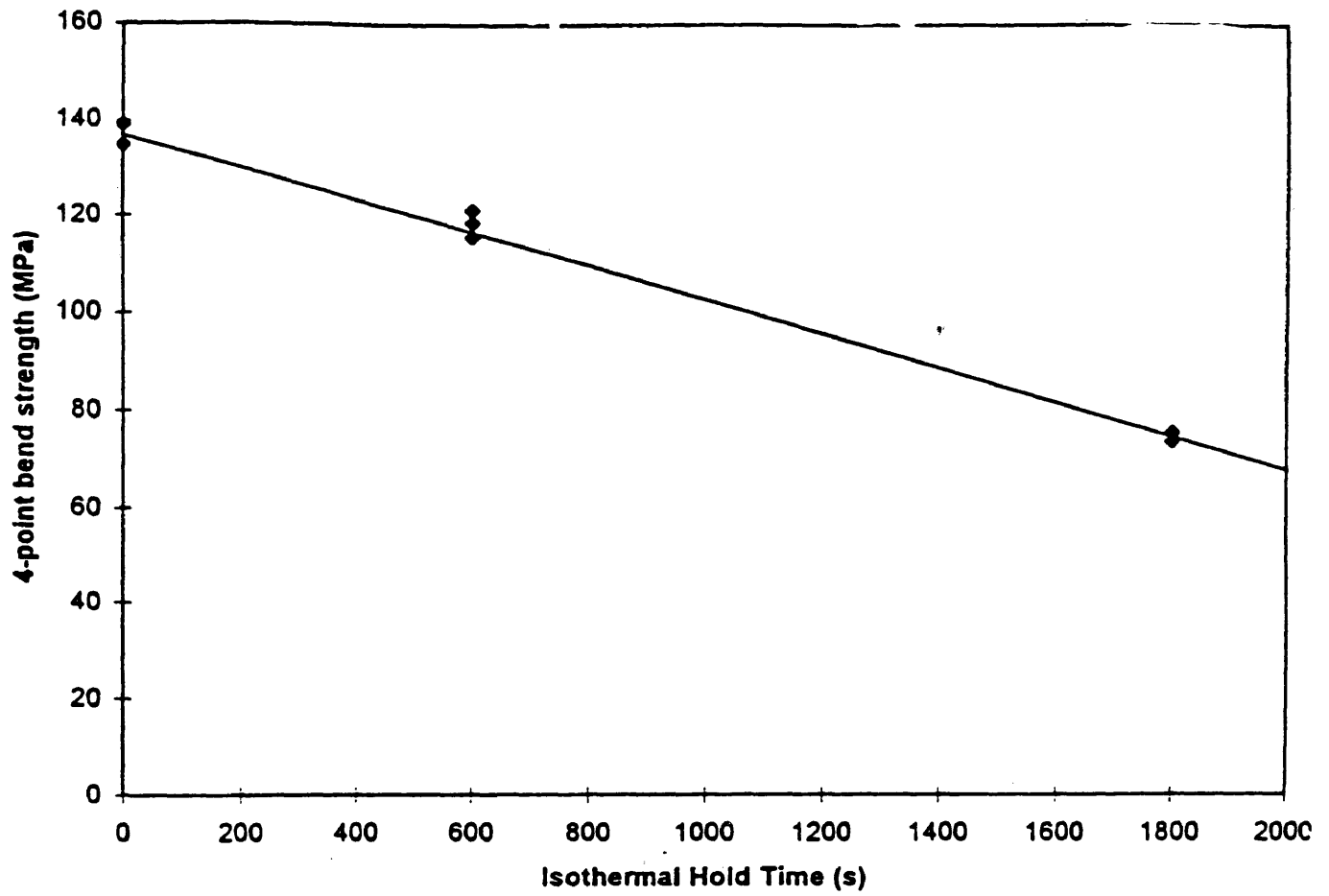


Figure 4.1: Four-point bend strength versus isothermal holding time for nickel/alumina joints with titanium-40 weight percent nickel interlayers at 1150°C.

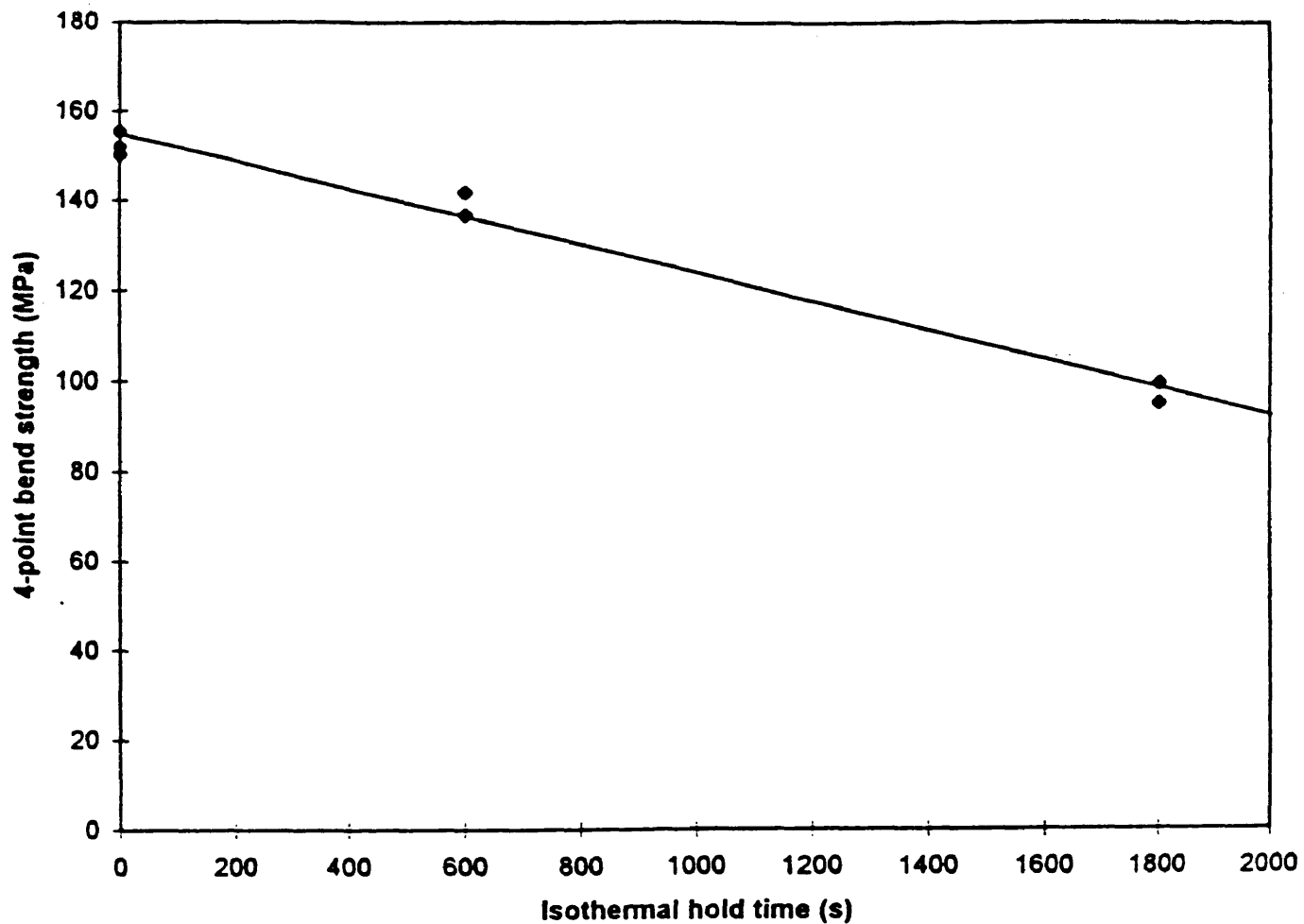


Figure 4.2: Four-point bend strength versus isothermal holding time for nickel/alumina joints with titanium-30 weight percent nickel interlayers at 1150°C.

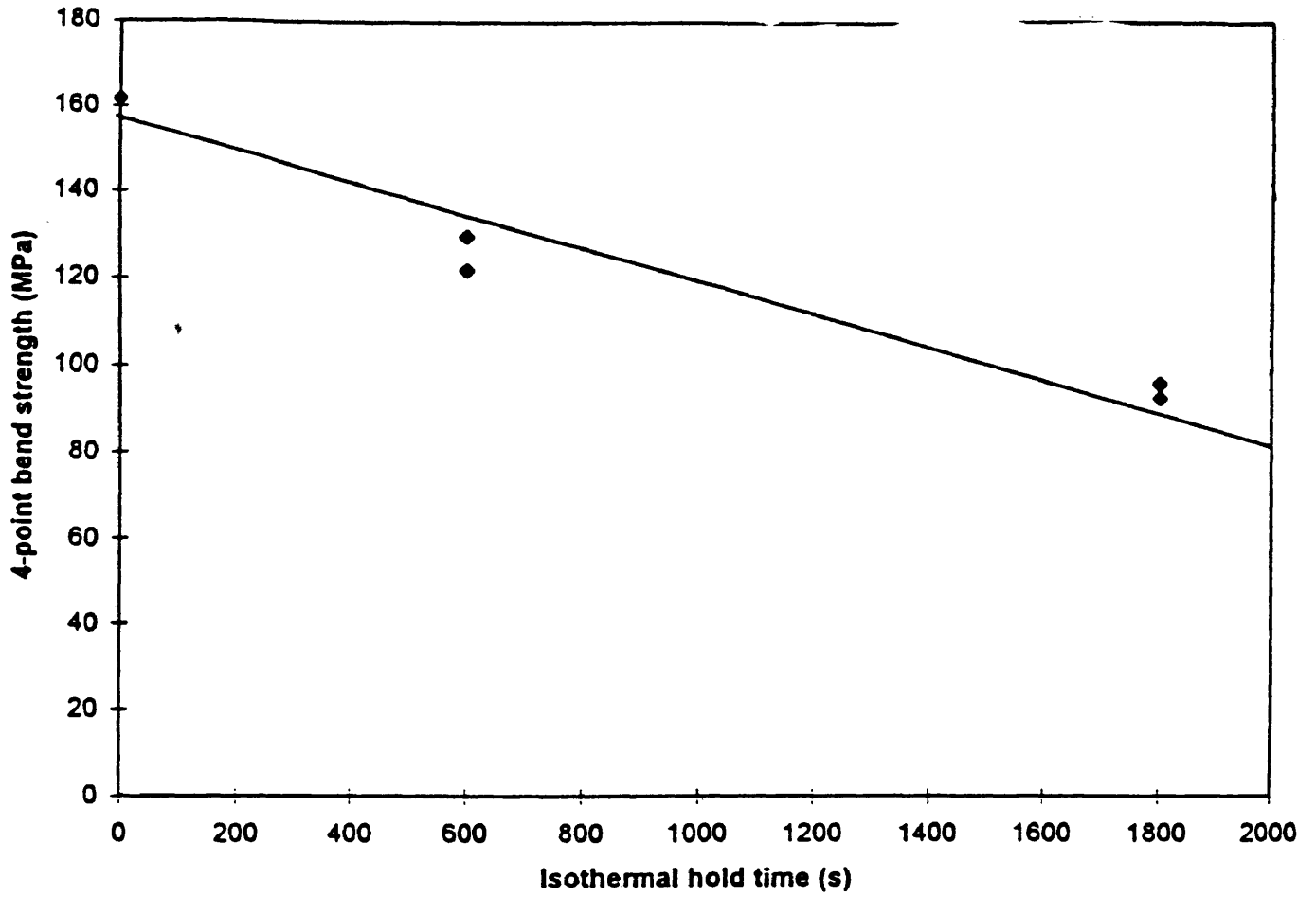


Figure 4.3: Four-point bend strength versus isothermal holding time for nickel/alumina joints with titanium-40 weight percent nickel interlayers at 1200°C.

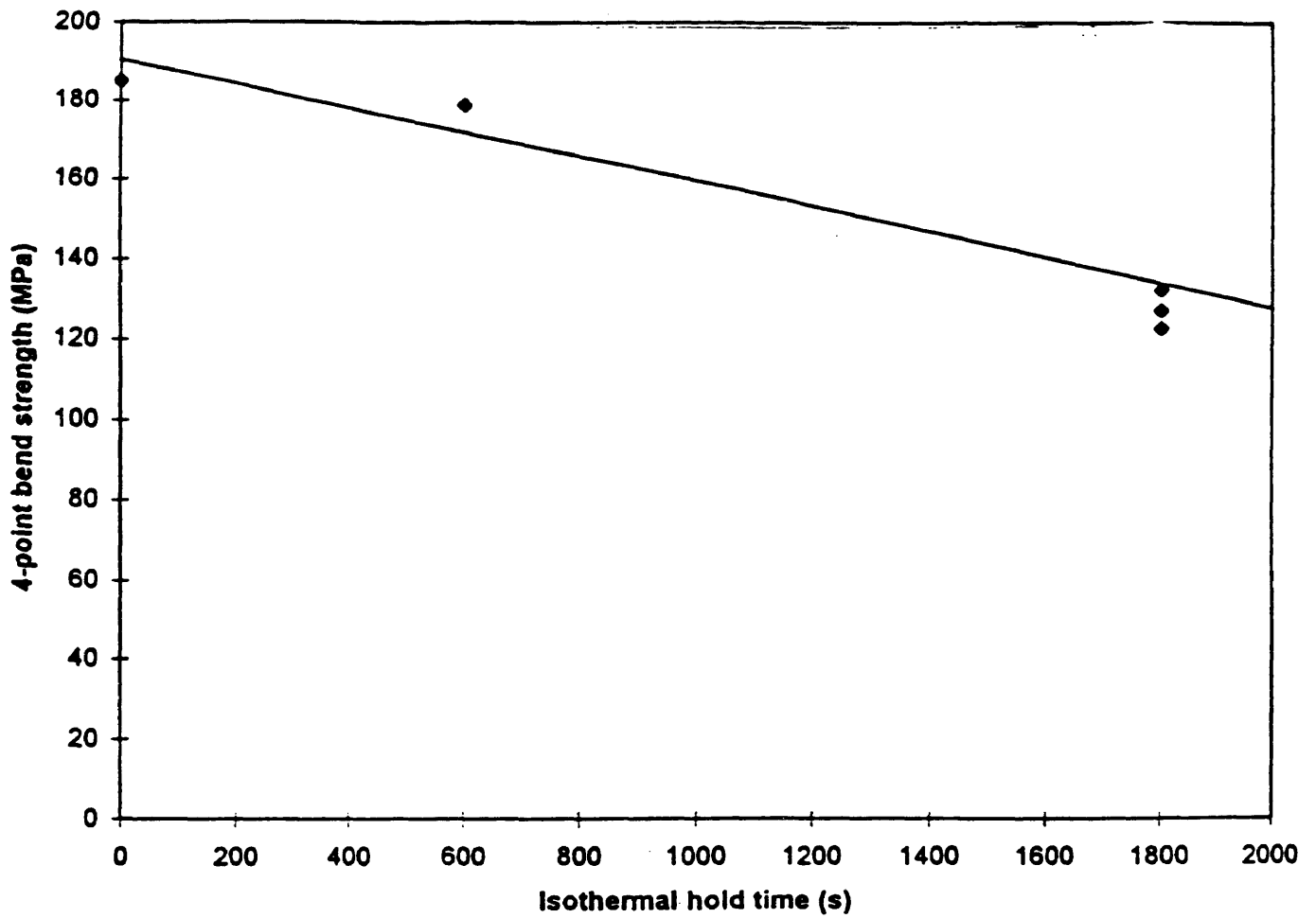


Figure 4.4: Four-point bend strength versus isothermal holding time for nickel/alumina joints with titanium-30 weight percent nickel interlayers at 1200°C.

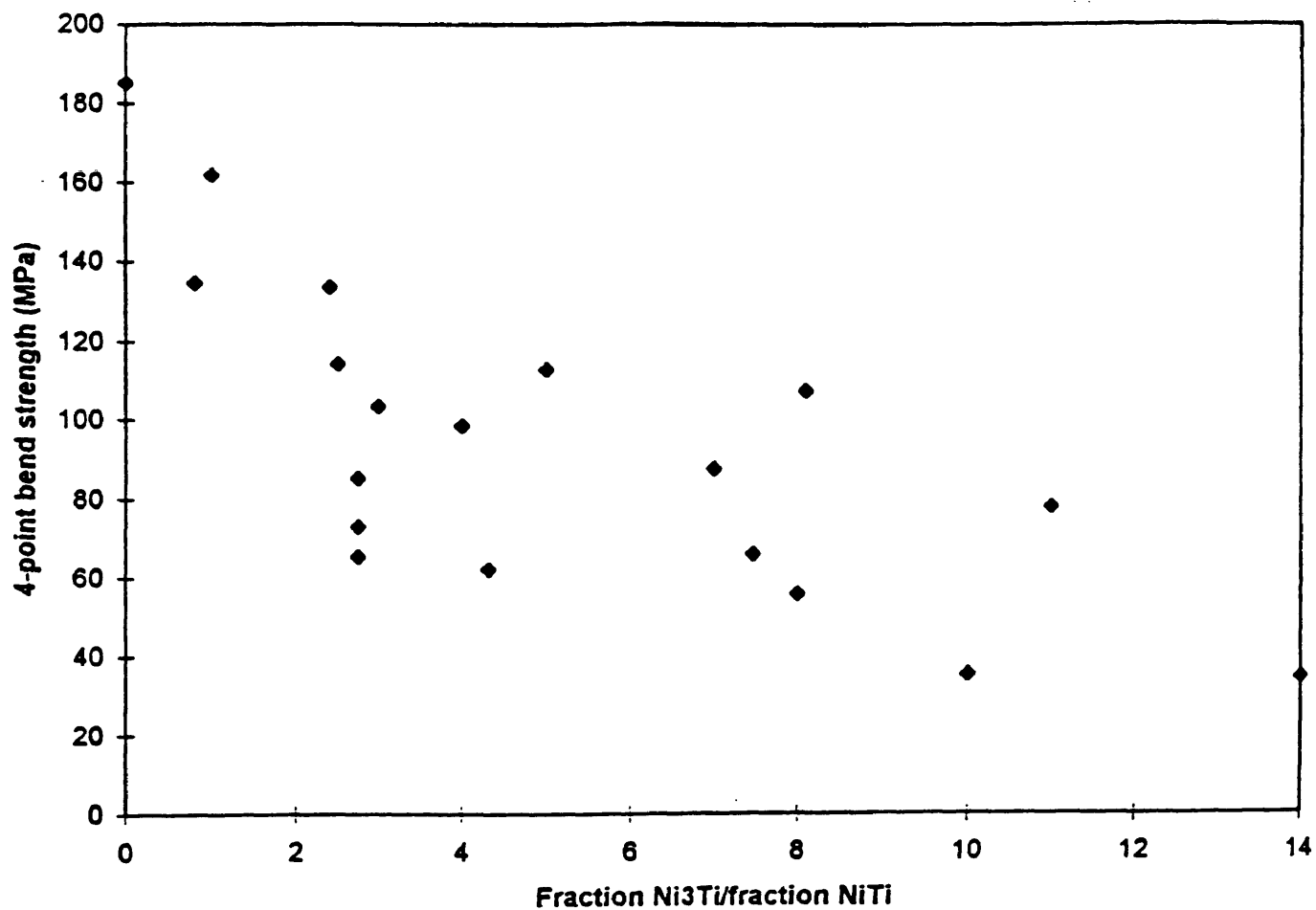


Figure 4.5: Four-point bend strength of nickel/alumina TLP brazed samples with titanium-30 weight percent nickel interlayers as a function of V_{Ni_3Ti}/V_{NiTi} .

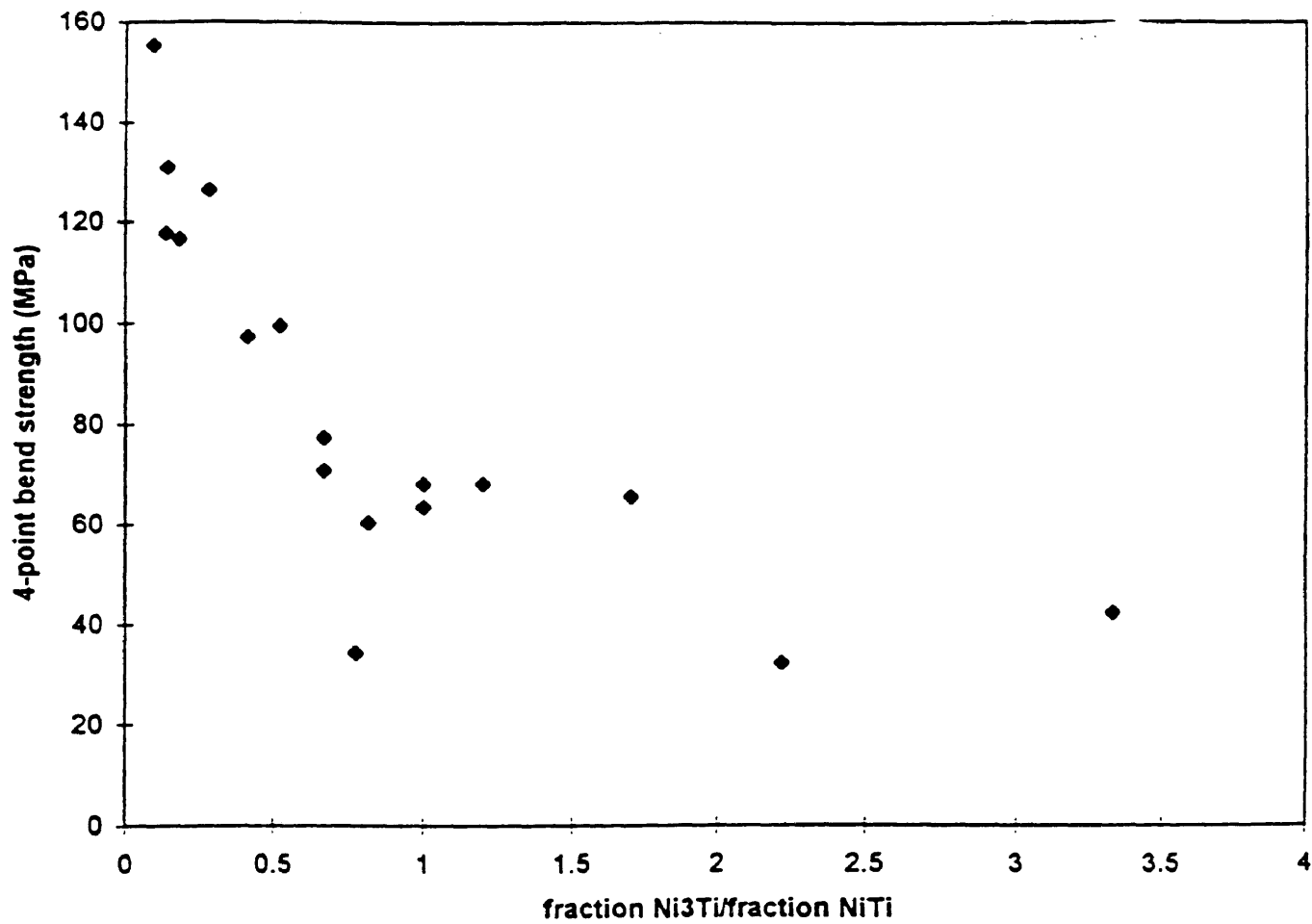


Figure 4.6: Four-point bend strength of nickel/alumina TLP brazed samples with titanium-40 weight percent nickel interlayers as a function of V_{Ni_3Ti}/V_{NiTi} .

shows the same plot for the sample with a 40 weight percent Ni-60 weight percent Ti interlayer composition.

It can be seen clearly that the highest bond strengths were obtained when the bond was predominantly NiTi. A maximum strength of 185 MPa was obtained in a bond that has only NiTi present. As more Ni₃Ti formed within the bond, the strength was seen to decrease. In samples with 30 weight percent Ni-70 weight percent Ti interlayers, the bond strength fell to fifty percent of the maximum when the fraction of Ni₃Ti was approximately four times that of NiTi. In samples with 40 weight percent Ni-60 weight percent Ti interlayers, the strength fell to fifty percent of the maximum when the fraction of Ni₃Ti was approximately equal to that of NiTi.

B. Compositional Profiles Microscopy

In the SEM, samples were analyzed using the EDS system to create compositional profiles across the nickel-ceramic interface for each sample. Figure 4.7 shows a representative profile of one the samples. As shown in Figure 4.7, each layer in the interface, such as NiTi or Ni₃Ti, can be easily identified. The thickness of each layer can also be measured on the profile. These thicknesses were correlated with the processing characteristics by plotting the thickness of each layer against the time at temperature for each condition.

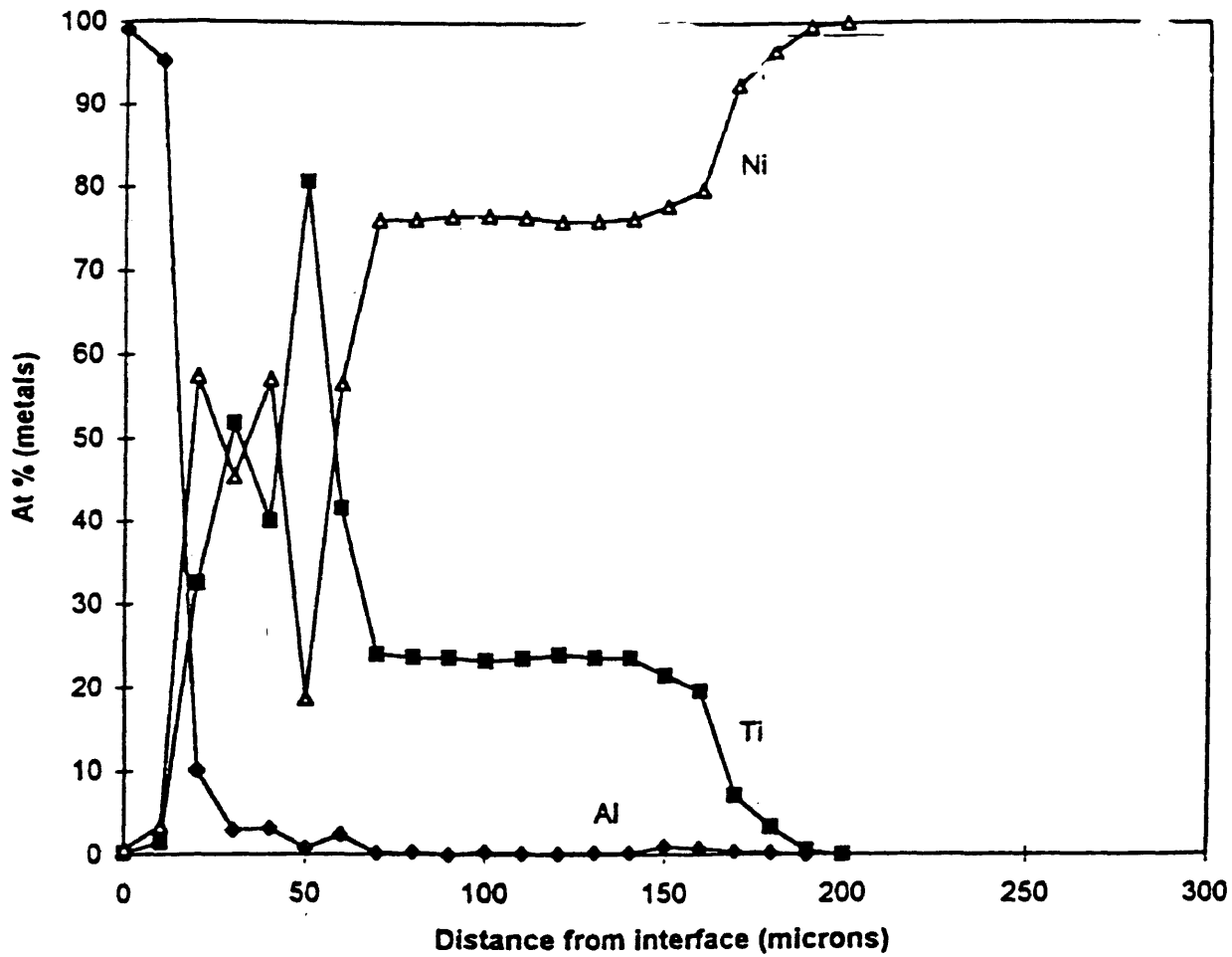


Figure 4.7: Representative compositional profile created with data from SEM analysis of nickel/alumina TLP brazed joints.

C. Fracture Surface Analysis

The fracture surfaces of the broken four-point bending samples were analyzed to determine the fracture behavior of the interface. It was determined that in every case, the fracture occurred in the ceramic material close to the interface. This information points to the presence of residual stresses within the joint, as a result of the joint formation. This fracture behavior and the presence of residual stresses will be further explained in the Discussion section, below.

V Discussion

In this section, the results obtained from the experiments are discussed in four sections. The first important result was the correlation found between the microstructure of the bond and the resulting bond strength. Next, the fracture behavior of the bonds was analyzed and interpreted. Third, the bond development during the brazing cycle was analyzed. Lastly, the kinetic analysis of the formation of Ni_3Ti in the bond was analyzed.

A. Microstructure-Strength Correlation

As shown in the previous section, compositional profiles were developed for each sample with data obtained from SEM analysis. From these profiles, the thickness of NiTi and Ni_3Ti in each sample were measured. Because the interfaces within the bond were planar, the thickness of a given layer within a given sample remained constant. This situation allowed the determination of the relative fractions of NiTi and Ni_3Ti present in each sample to be determined.

As mentioned in the previous section, the highest bond strengths were obtained when the bond was predominantly NiTi. The presence of only NiTi in the bond gave a maximum strength of 185 MPa. This value is approximately 45 percent of the bend strength of pure monolithic alumina. As the amount of Ni_3Ti in the bond increased, the

bond strength of the bond decreased. In sample with 30 weight percent Ni-70 weight percent Ti interlayers, the bond strength fell to fifty percent of the maximum when the fraction of Ni_3Ti was approximately four times that of NiTi. In sample with 40 weight percent Ni-60 weight percent Ti interlayers, the strength fell to fifty percent of the maximum when the fraction of Ni_3Ti was approximately equal to that of NiTi.

The reason for this behavior can be explained by the differences in the behavior of NiTi and Ni_3Ti . NiTi is known to be a ductile phase, which could absorb some of the deformation that occurs in the bond when mechanically loaded. Ni_3Ti , which is a brittle intermetallic compound, cannot absorb the deformation, which will result in a lower strength bond.

B. Fracture Behavior

As mentioned in the previous section, the fracture surfaces of each sample were analyzed in the SEM to determine how each sample broke. Each sample fractured within the alumina, not within the nickel/alumina bond itself. This behavior can be explained by the presence of residual stresses within the ceramic after the brazing cycle is completed.

Figure 5.1 shows a schematic diagram of what happens to the sample as it cools from the brazing temperature to room temperature. Due to the different thermal expansion characteristics of the alumina and the nickel and nickel-titanium, residual

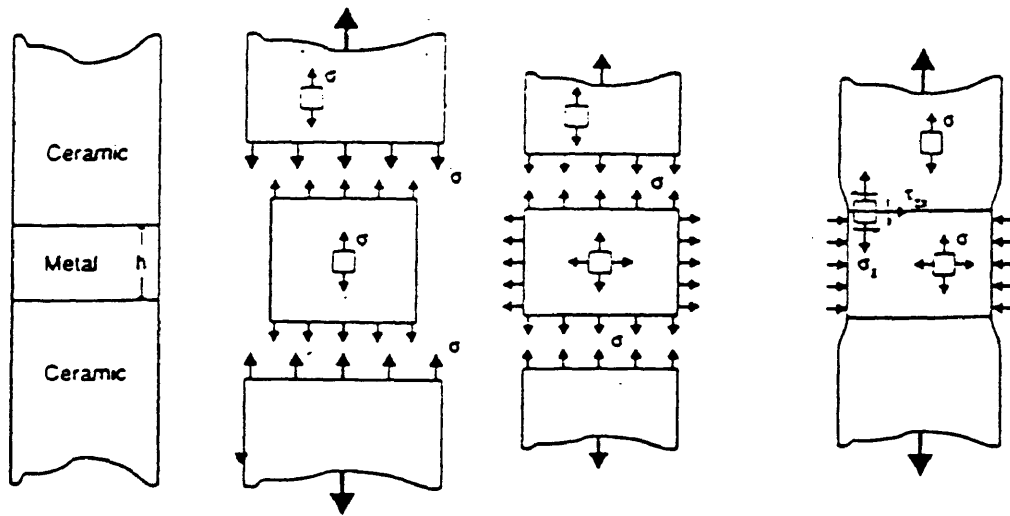


Figure 5.1: Schematic of cooling of ceramic/metal brazed joint from brazing temperature to room temperature.

stresses build up at the interface. Because of its ductility, NiTi is better able to absorb these stresses than Ni₃Ti.

The residual stresses are not completely removed by the presence of NiTi. In samples that have only NiTi present, a maximum bond strength of 185 MPa was achieved. This strength value would correspond to the smallest residual stresses possible under these conditions. Pure alumina bars were mechanically tested, giving a strength of 360 MPa. This result proves that the residual stresses were not totally eliminated by NiTi.

C. Bond Development

An understanding of how the bond develops between the nickel and alumina during brazing is necessary to further analyze the transient liquid phase brazing process. To determine how the bond develops, the starting composition of the interlayer must be known. Using the nickel-titanium phase diagram, the starting composition was plotted, as shown in Figure 5.2.

During the brazing cycle, the interlayer composition changed as diffusion of the constituents occurred. Tracking these changes will give an idea of how the bond between the nickel and alumina forms, as well as shown the steps that determine the strength of the resulting joint.

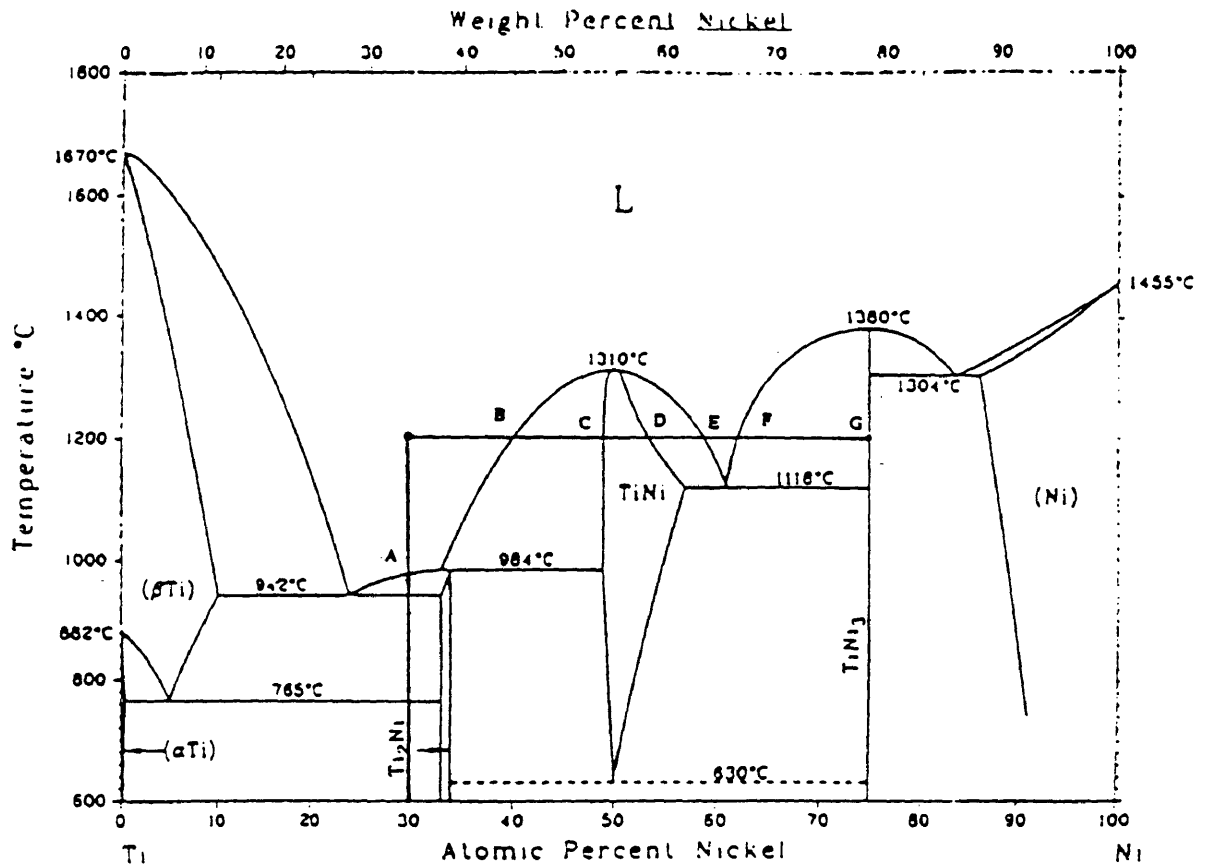


Figure 5.2: Nickel-titanium phase diagram with compositional changes as a result of the brazing cycle plotted.

Initially, the interlayer was a powder mixture of pure nickel and titanium, but as the temperature was increased to the brazing temperature, this layer became a liquid, shown on Figure 5.2 at point A. While liquid, diffusion of nickel and titanium into and out of the pure nickel layer resulted in the beginning of NiTi solidification, shown in Figure 5.2 at point B. Eventually, this layer became completely NiTi, leaving no liquid (Figure 5.2, point C). These steps occurred during the heating to the brazing temperature, as evidenced by the presence of the NiTi layer in samples with no holding time at the brazing temperature.

When the sample was held at the brazing temperature, more diffusion between the interlayer and the pure nickel occurred. This behavior resulted in the formation of another liquid phase, shown in Figure 5.2 at point D. This liquid continued to form until the interlayer was again totally liquid, as shown in Figure 5.2 at point E. The composition of the interlayer continued to change as a result of the diffusion until Ni_3Ti began to form. The brazing process was seen to proceed to this point within 600 seconds. When held for longer than 600 seconds, the interlayer continued to solidify as Ni_3Ti until the layer is totally Ni_3Ti . The last two steps are shown in Figure 5.2 at points F and G. The diffusion of nickel through Ni_3Ti is much slower than through the liquid layer and the brazing process is effectively completed at this point. Samples that were held for 1800 seconds showed 100 percent Ni_3Ti interlayers, meaning that the completion of the Ni_3Ti formation

occurs between 600 and 1800 seconds. As shown by samples with longer hold times, once the Ni_3Ti layer forms, no other compositional changes take place.

As was discussed above, the presence of Ni_3Ti had a large effect on the bond strength. A kinetic analysis of the growth of the Ni_3Ti layer will be presented in the next section.

D. Kinetic Analysis of Ni_3Ti

To gain a better understanding of the TLP process, an investigation of the thickening kinetics of the Ni_3Ti layer was undertaken. A separate analysis was made for both of the different initial interlayer compositions. Figures 5.3, 5.4, and 5.5 show the thickness of the Ni_3Ti layer as a function of the square root of the isothermal holding time for the interlayer composition of 30 weight percent Ni-70 weight percent Ti at 1150C, 1200C, and 1250°C, respectively. Figures 5.6, 5.7, and 5.8 show the same thing for the interlayer composition 40 weight percent Ni-60 weight percent Ti.

For an initial analysis, the growth of Ni_3Ti was assumed to be parabolic in nature. For this reason, the thicknesses were plotted against the square root of the isothermal holding time. As can be seen in the plots, the data give linear results, confirming that the growth is indeed parabolic in nature. The error bars represent a 95 percent confidence interval, or two standard deviations of the thickness measurement. No error bars are

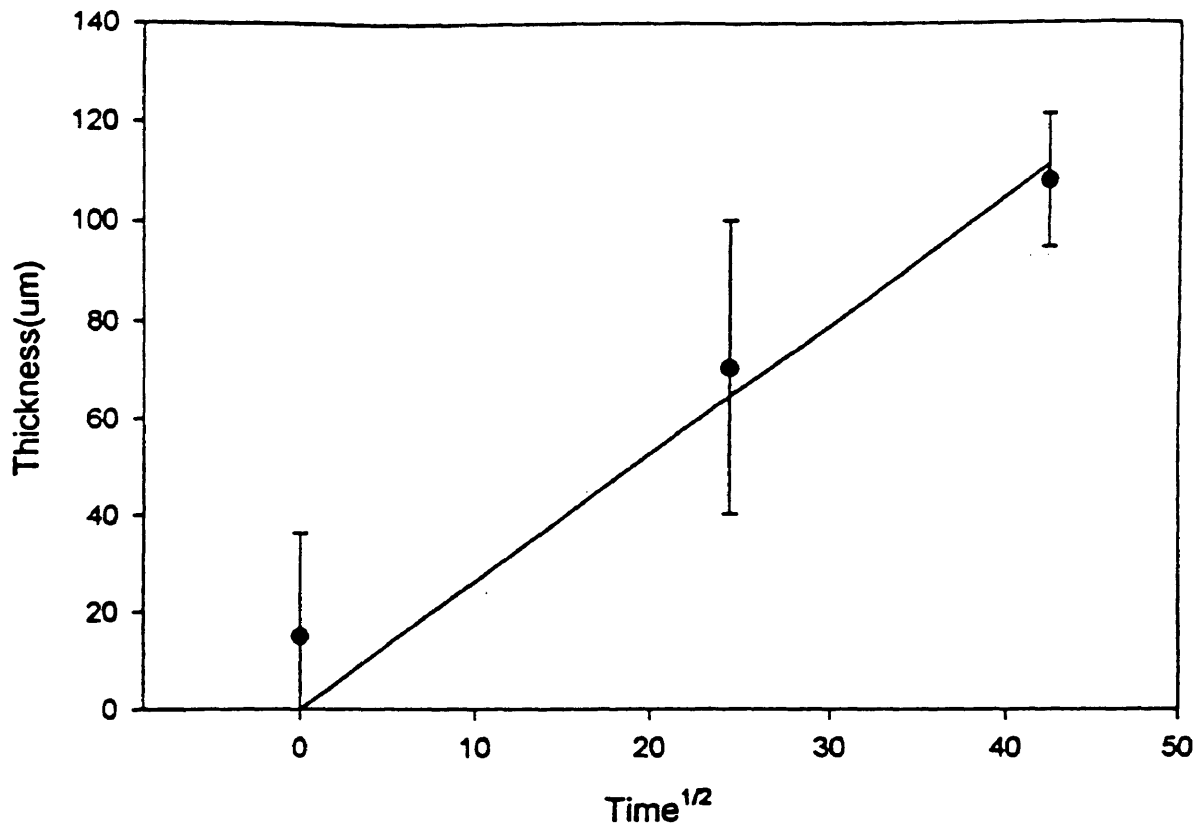


Figure 5.3: Thickness of Ni₃Ti layer versus time^{1/2} for nickel/alumina samples with titanium-30 weight percent nickel interlayers brazed at 1150°C.

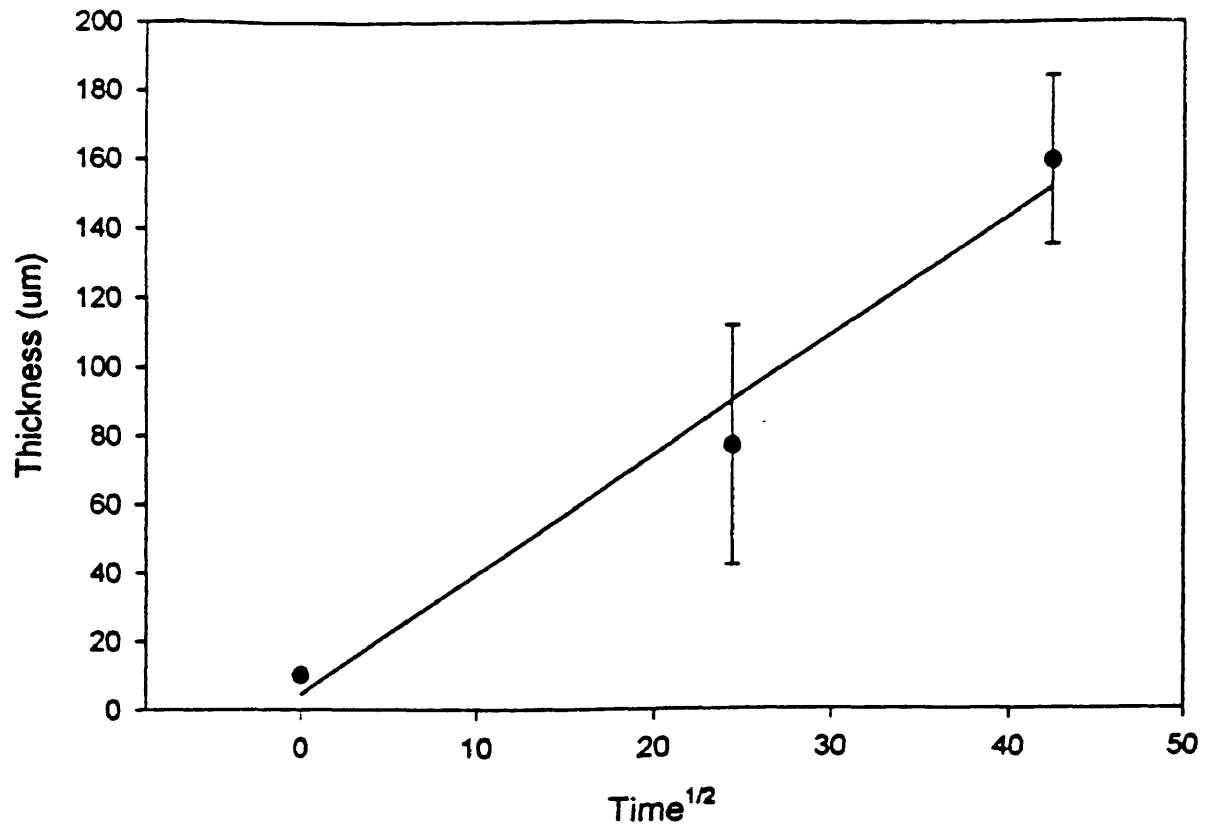


Figure 5.4: Thickness of Ni_3Ti layer versus time^{1/2} for nickel/alumina samples with titanium-30 weight percent nickel interlayers brazed at 1200°C.

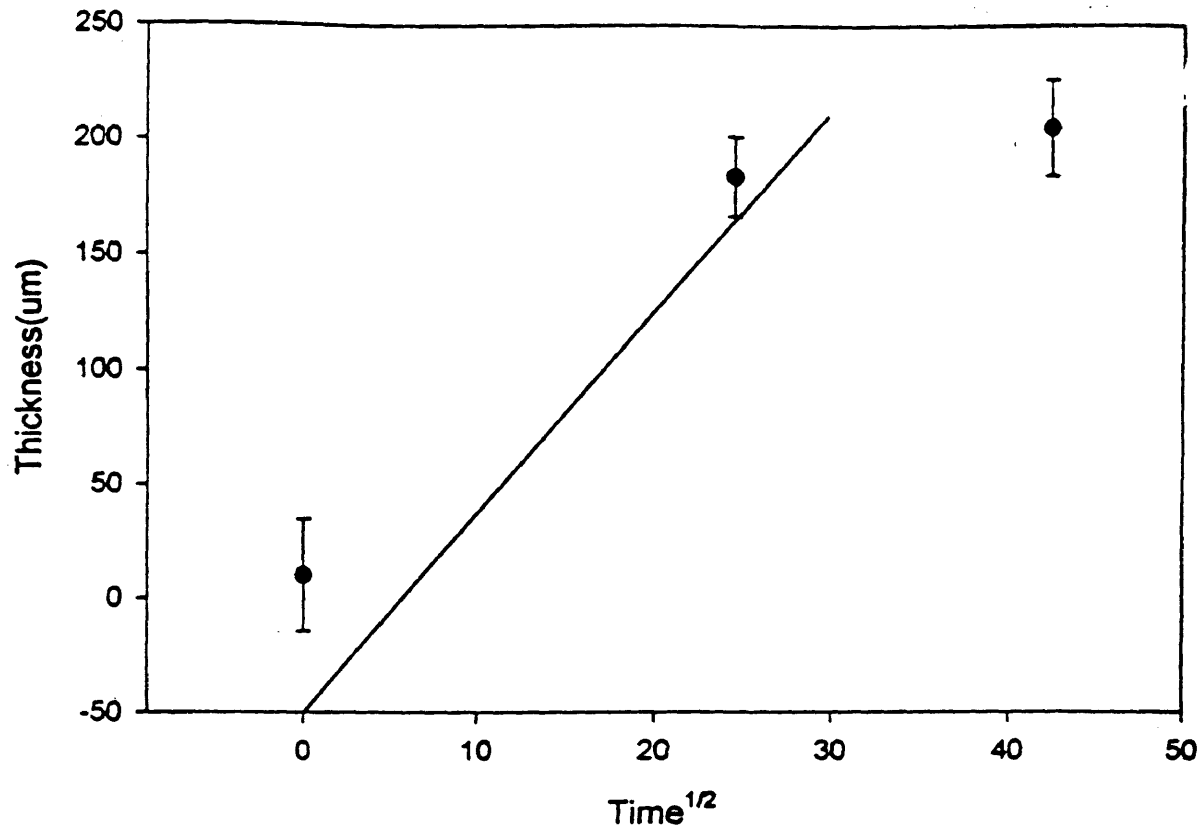


Figure 5.5: Thickness of Ni₃Ti layer versus time^{1/2} for nickel/alumina samples with titanium-30 weight percent nickel interlayers brazed at 1250°C.

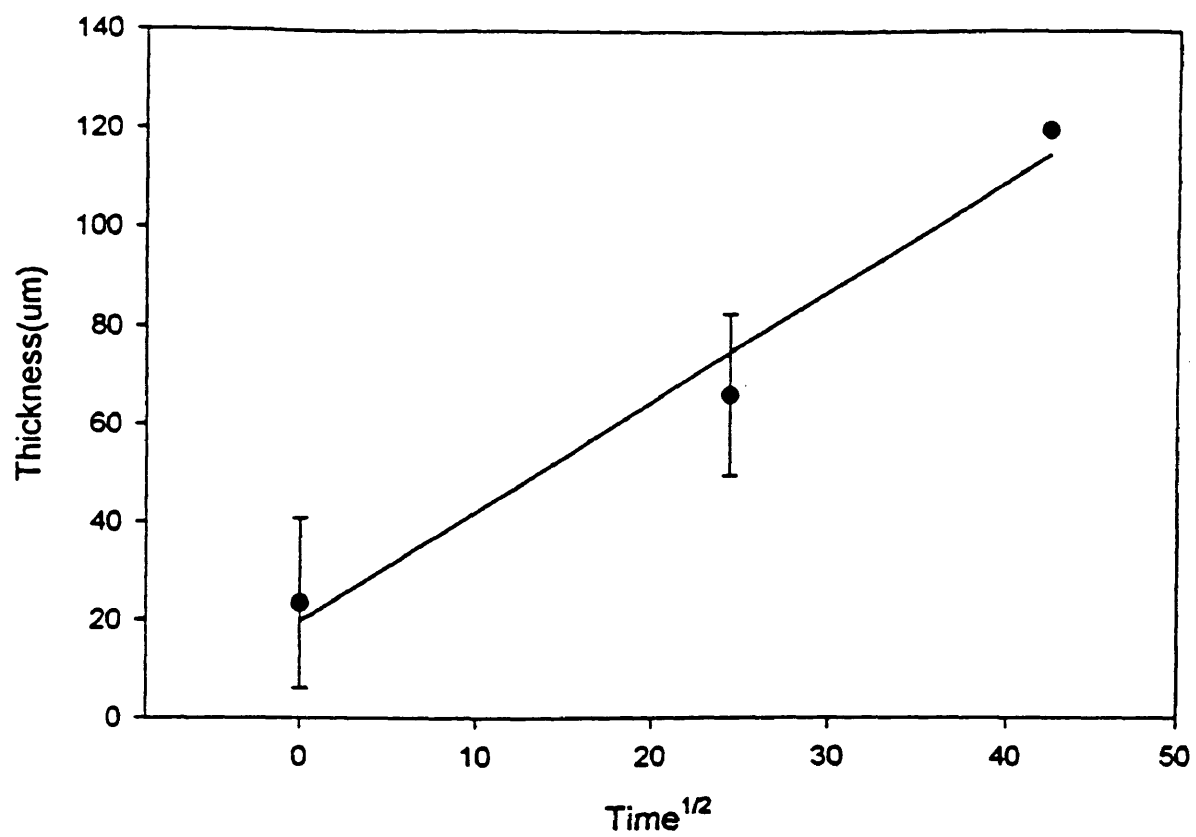


Figure 5.6: Thickness of Ni₃Ti layer versus time^{1/2} for nickel/alumina samples with titanium-40 weight percent nickel interlayers brazed at 1150°C.

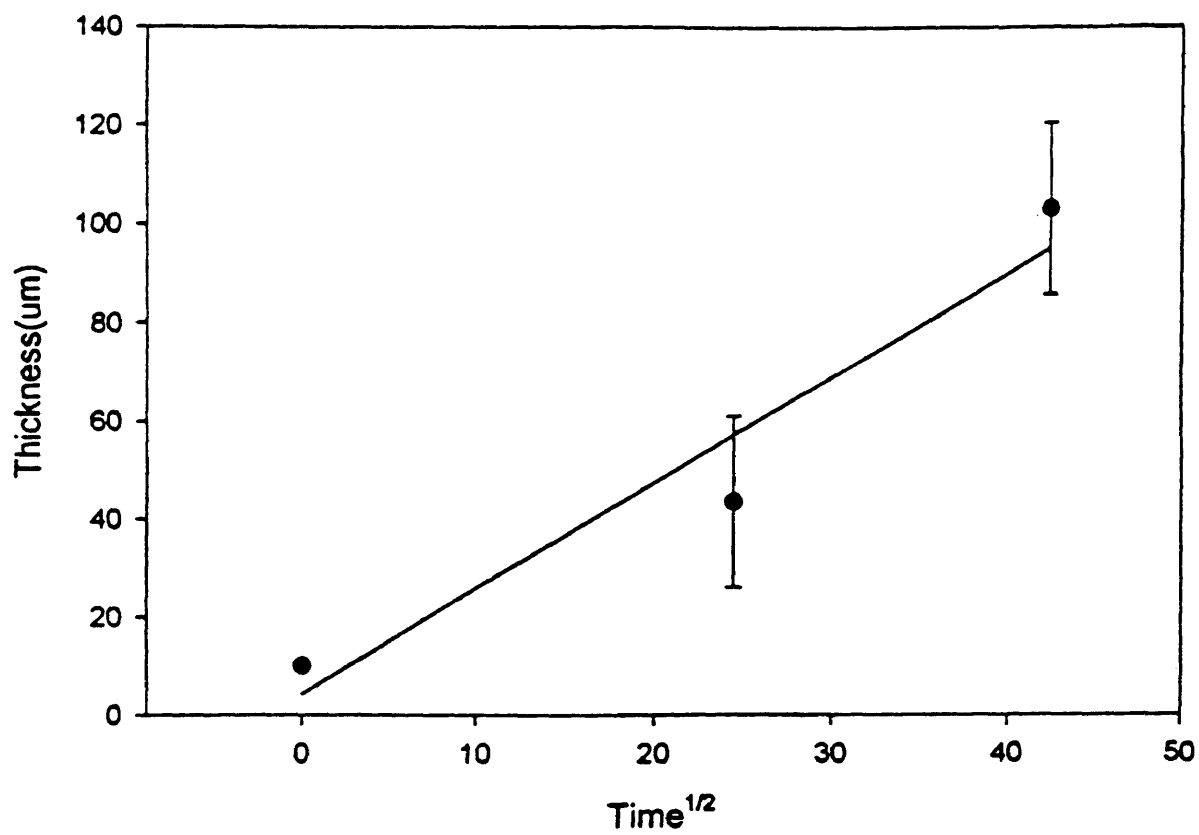


Figure 5.7: Thickness of Ni_3Ti layer versus time ^{1/2} for nickel/alumina samples with titanium-40 weight percent nickel interlayers brazed at 1200°C.

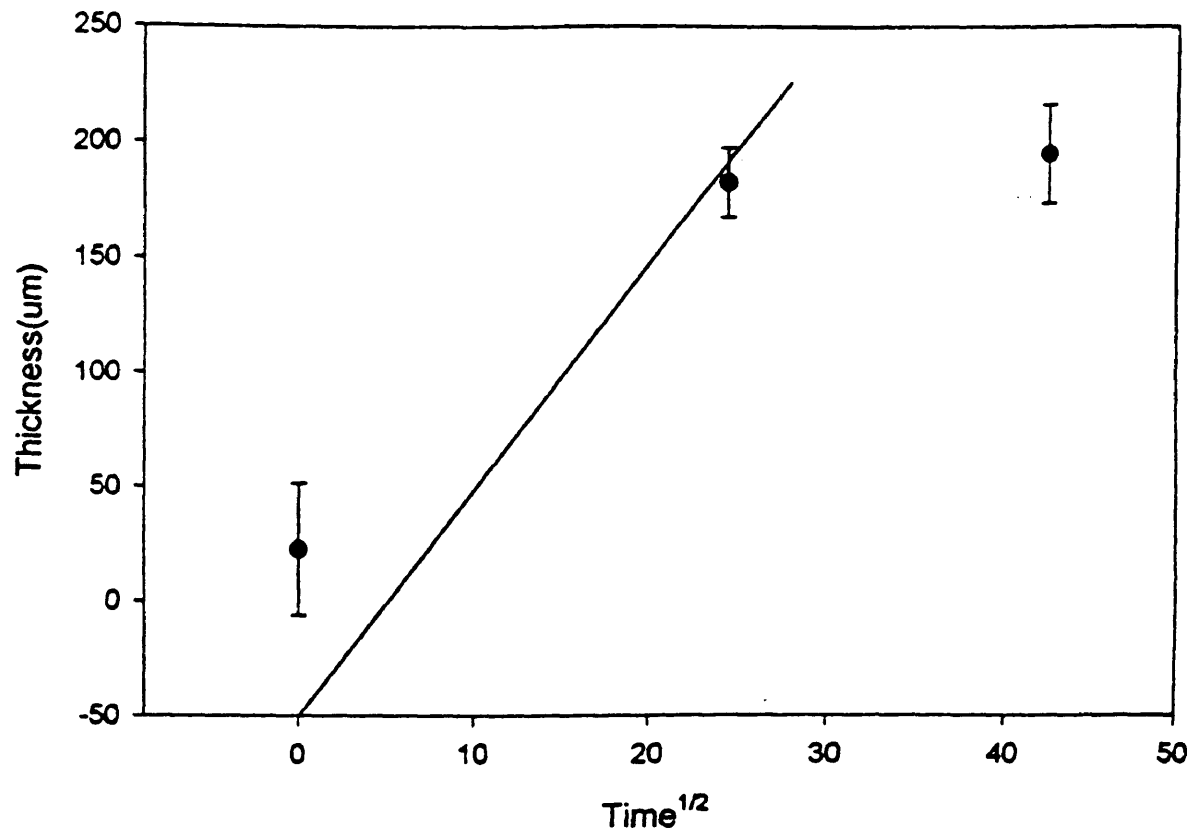


Figure 5.8: Thickness of Ni₃Ti layer versus time^{1/2} for nickel/alumina samples with titanium-40 weight percent nickel interlayers brazed at 1250°C.

shown for points where twice the standard deviation was a smaller dimension than the size of the plotting symbol.

An apparent reaction rate constant for the growth of Ni₃Ti, k , was calculated from the thickening kinetics data. An intrinsic rate refers to the growth of a single layer without influence from neighboring layers. The intrinsic rate constant is representative of the atomistic processes contributing to the formation of a single layer. An apparent rate refers to the growth of a layer with influences from the neighboring layers.

An expression for the apparent reaction rate constant can be written as:

$$k = \frac{\text{Ni}_3\text{Ti layer thickness}^2}{\text{Isothermal holding time}} \quad (67)$$

An Arrhenius-type activation energy analysis can be used to calculate the temperature dependence of the apparent reaction rate constant, k .

The apparent rate constant can be expressed as:

$$k = k_0 \exp\left(\frac{-Q}{RT}\right) \quad (68)$$

A plot of the logarithm of the reaction rate constant versus the inverse absolute temperature can be used to calculate the apparent activation energy of the Ni_3Ti growth process. Figures 5.9 and 5.10 are plots of the logarithm of the reaction rate constants versus inverse absolute temperature for 30 weight percent Ni-70 weight percent Ti and 40 weight percent Ni-60 weight percent Ti interlayers, respectively. The slope of the line on Figure 5.9 indicates an activation energy of 130 kJmole^{-1} . The slope from Figure 5.10 indicates an activation energy of 135 kJmole^{-1} .

This activation energy was interpreted to be the activation energy for the diffusion of nickel through Ni_3Ti .

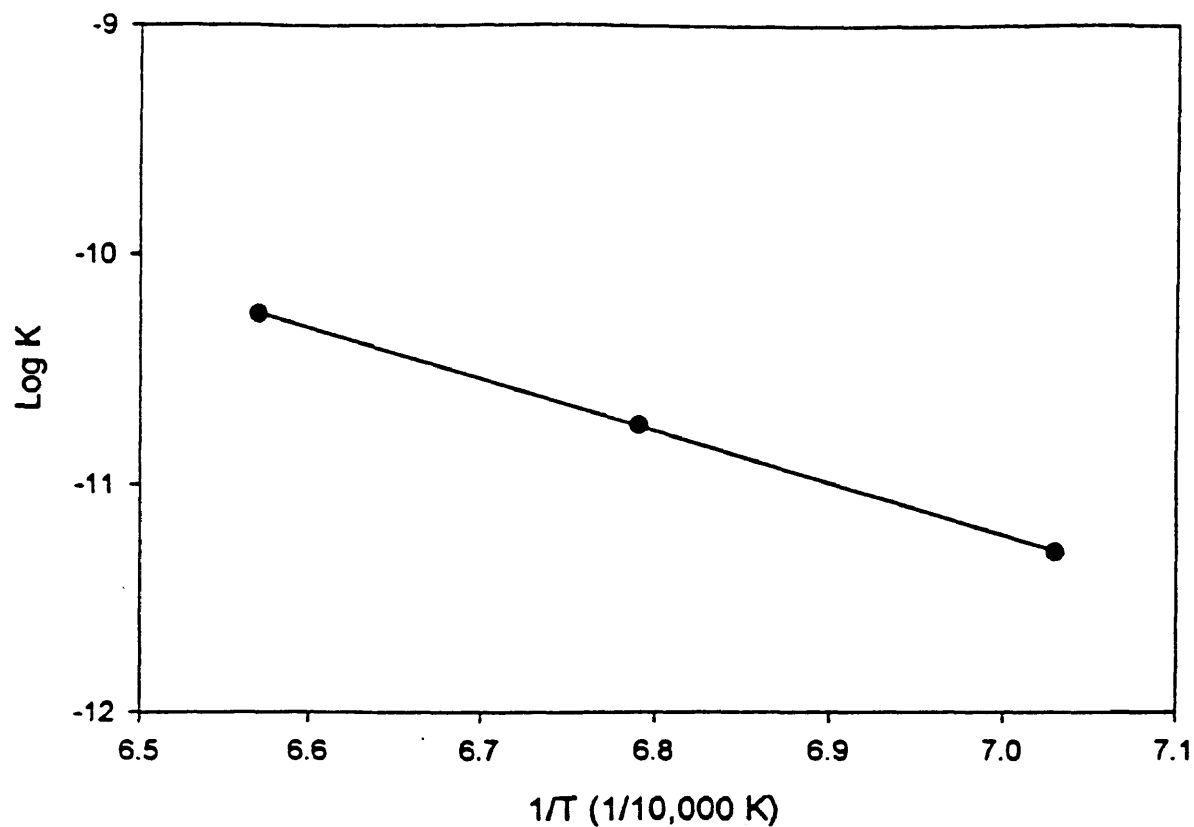


Figure 5.9: Temperature dependence of the reaction rate constant, K : logarithm of K as a function of inverse absolute temperature for the growth of Ni_3Ti in nickel/alumina TLP brazed joints with titanium-30 weight percent nickel interlayers.

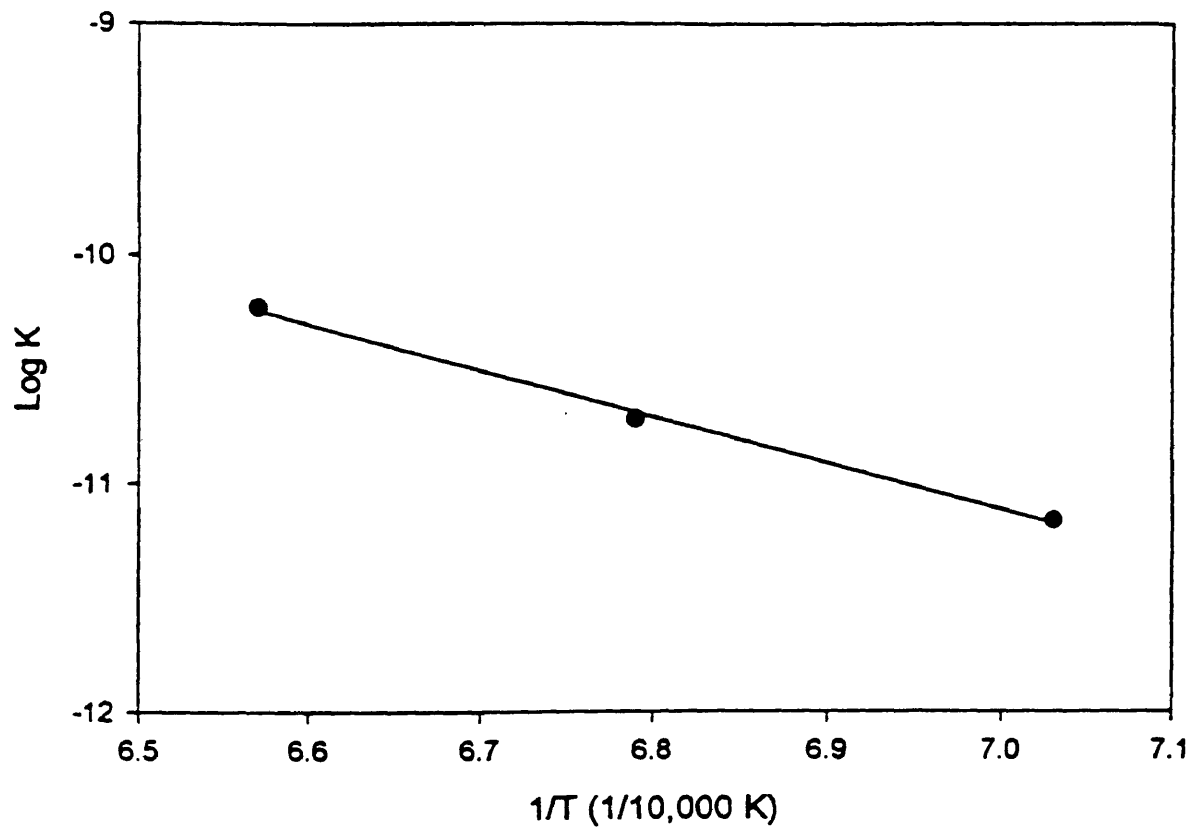


Figure 5.10: Temperature dependence of the reaction rate constant, K : logarithm of K as a function of inverse absolute temperature for the growth of Ni_3Ti in nickel/alumina TLP brazed joints with titanium-40 weight percent nickel interlayers.

VI Conclusions

Nickel was successfully bonded to alumina using transient liquid phase brazing with nickel-titanium interlayers. The presence of ductile NiTi in the brazed joint proved beneficial to the joint strength, while the presence of Ni₃Ti was shown to be detrimental to the strength. This was observed to be the result of the residual stresses in the joint which the NiTi phase was able to absorb. However, the Ni₃Ti phase was not able to deal with this residual stress.

The growth of the Ni₃Ti layer was shown to be controllable by modifying the experimental parameters of brazing time and brazing temperature. The growth behavior of the Ni₃Ti phase was determined to be parabolic in nature. The activation energy of this process was determined to be 130 kJmol⁻¹ for an interlayer composition of titanium-30 weight percent nickel, and 135 kJmol⁻¹ for an interlayer composition of titanium-40 weight percent nickel. This result was interpreted to be the activation energy for the diffusion of nickel through Ni₃Ti.

VII REFERENCES

1. Massalski, T.B. (Ed.), Binary Alloy Phase Diagrams Vol. 3, ASM International, Materials Park, OH (1990), p. 2875.
2. Meier, A., Ph.D. Thesis, "Modelling of the Spreading Kinetics of Reactive Brazing Alloys on Ceramic Substrates: Copper-Titanium and Silver-Titanium Alloys on Polycrystalline Alumina", Colorado School of Mines, T-4665, November 1994.
3. Loehman, R., "Interfacial Reactions in Ceramic-Metal Systems", Ceram Bull 68 [4] (1989), pp. 891-896.
4. Nicholas, M.G., and R.J. Lee, "Joining Dissimilar Materials", Metals and Materials 5 [6] (June 1989), pp. 348-351.
5. Popper, P., "The Joining of Industrial Ceramics to Metals", In: Energy and Ceramics, Proceedings of the 4th International Meeting on Modern Ceramics Technologies, Saint-Vincent, Italy, 28-31 May 1979, P. Vincenzini (ed.), Elsevier Scientific Publishing, Amsterdam, 1980.
6. Mizuhara, H., "Vacuum Brazing Ceramics to Metals", Adv Mat and Processes in Metal Progress (Feb 1987), pp. 53-55.
7. Kapoor, R.R., and T.W. Eagar, "Oxidation Behavior of Silver-and Copper Based Brazing filler Metals for Silicon Nitride/Metal Joints" J Amer Ceram Soc 72 [3] (1989), pp. 448-454.
8. Moorehead, A.J., and H. Keating, "Direct Brazing of Ceramics for Advanced Heavy-Duty Diesels", Welding J 65 [10] (1986), pp. 17-31.
9. Musikant, S., What Every Engineer Should Know About Ceramics Marcel Dekker, Inc., New York (1991), Chapters 7, 12, and 13.
10. Sigl, L.S., P.A. Matanga, B.J. Dalgeish, R.M. Meeking and A.G. Evans, "On the Toughness of Brittle Materials Reinforced with a Ductile Phase", Acta Met 36 [4] (1988), pp. 945-953.

11. Ritland, M.R., and D.W. Readey, "Alumina-Copper Composites by Vapor Sintering", Ceram Eng and Sci Proc 14 [9-10] (1993), pp. 896-907.
12. Nicholas, M.G., R.M. Crispin and D.A. Ford, "Some Effects of Surface Texture on Melt-Mold Interactions During Investment Casting", Brit Ceram Soc Proceeding 34 (Aug 1984), pp. 163-172.
13. Bartlett, A., A.G. Evans and M. Rühle, "Residual Stress Cracking of Metal/Ceramic Bonds", Acta Met 39 [7] (1991), pp. 1579-1585.
14. Suganuma, K., "Recent Advances in Joining Technology of Ceramics to Metals", ISIJ Int 30 [12] (1990), pp. 1046-1058.
15. Morita, M., K. Suganuma, and T. Okamoto, "Effect of Pre-Treatment on Silicon Nitride Joining with Alumina Braze", J Mat Sci Letters 6 (1987), pp. 474-476.
16. He, M.Y., and H.G. Evans, "The Strength and Fracture of Metal/Ceramic Bonds" Acta Met 39 [7] (1991), pp. 1587-1593.
17. Tvergaard, V., "Failure by Ductile Cavity Growth at a Metal-Ceramic Interface", Acta Met 39 [3] (1991), pp. 419-426.
18. Elssner, G., and G. Petzow, "Metal/Ceramic Joining", ISIJ Int 30 [12] (1990), pp. 1011-1032.
19. Suganuma, K., T. Okamoto, M. Kozumi, and M. Shimada, "Joining of Silicon Nitride to Silicon Nitride and to Invar Using an Aluminum Interlayer", J Mat Sci 22 (1987), pp. 1359-1364.
20. Adamson, A.W., Physical Chemistry of Surfaces 5th ed., John Wiley & Sons, Inc., New York (1990), Chapters II, III, VII, X.
21. Hiemenz, P.C., Principles of Colloid and Surface Chemistry 2nd ed., Marcel Dekker, Inc., New York (1986), pp. 288-335.
22. de Gennes, P.G., "Wetting: Statics and Dynamics", Reviews of Modern Physics 57 [3.1] (July 1985), pp. 827-863.

23. Fisher, L.R., "Measurement of Small Contact Angles for Sessile drops", J Colloid Int Sci 72 [2] (1979), pp. 200-205.
24. Mortensen, A. "Interfacial Phenomena in the Solidification Processing of Metal Matrix Composites", Mat Sci Eng A135 (1991), pp. 1-11.
25. Ngan, C.G., and E.B. Dussan V, "On the Nature of the Dynamic Contact Angle: An Experimental Study", J Fluid Mech 118 (1982), pp. 27-40.
26. Myers, Drew, Surfaces, Interfaces and Colloids: Principles and Applications, VCH Publishers, New York (1991), Chapter 17.
27. Tamai, Y., and K. Aratani, "Experimental Study of the Relation Between Contact Angle and Surface Roughness", J Phys Chem 76 [22] (1972), pp. 3267-3271.
28. Sagiorgi, R., M.L. Muolo, and A. Bellosi, "Wettability of Hot-Pressed Silicon Nitride Materials by Liquid Copper", Mat Sci and Eng A103 (1988), pp. 277-283.
29. Aksay, I.A., C.E. Hoge, and J.A. Pask, "Wetting under Chemical Equilibrium and Non-Equilibrium Conditions" J Phys Chem 78 [12] (1974), pp. 1178-1183.
30. Loehman, R.E., and A.P. Tomsia, "Reactions of Ti and Zr with AlN and Al₂O₃", Acta Metall Mater 40 (suppl 1992), pp. 575-583.
31. Laurent, V., D. Chatain, and N. Eustathopoulos, "Wettability of SiO₂ and Oxidized SiC by Aluminum", Mat Sci Eng A135 (1991), pp. 89-94.
32. Xue, X.M., J.T. Wang and M.X. Quan, "Wettability and Spreading Kinetics of Liquid Aluminum on Boron Nitride", J Mater Sci 26 (1991), pp. 6391-6395.
33. Shimbo, M., M. Naka, and I. Okamoto, "Wettability of Silicon Carbide by Aluminum, copper and Silver", J Mat Sci Letters 8 (1987), pp. 663-666.
34. Choh, T. and T. Oki, "Wettability of SiC to Aluminum and Aluminum Alloys", Mat Sci Tech 3 (May 1987), pp. 378-385.
35. Rocher, J.P., J.M. Quenisset, R. Naslain, "Wetting Improvement of Carbon or Silicon Carbide by Alloys Based on K₂ZrF₆ Surfaces Treatment: Application to Composites Materials Casting", J Mater Sci 24 [8] (June 1989), pp. 2697-2703.

36. Laurent, V., D. Chastian and N. Eustathopoulos, "Wettability of SiC by Aluminum and Al-Si Alloys", J Mat Sci 22 (1987), pp. 244-250.
37. Eustathopoulos, N., D. Chatain and L. Courdier, "Wetting and Interfacial Chemistry in Liquid Metal-Ceramic Systems" Mat Sci and Eng A135 (1991), pp. 83-88.
38. Li, J.G., "Wetting and Interfacial Bonding in Liquid Metal/Solid Ceramic Systems". Composite Interfaces 1 [1] (1993), pp. 37-53.
39. Kristalis, P., I. Courdier, and N. Eustathopoulos, "Contribution to the Study of Reactive Wetting in the CuTi/Al₂O₃ System", J Mat Sci 26 (1991), pp. 3400-3408.
40. Mizuhara, H., and K. Mally, "Ceramic-to-Metal Joining with Active Brazing filler Metal", Welding J 64 [10] (1985), pp. 27-32.
41. Selverin, J.H., and S. Kang, "Ceramic-to-Metal Joints Brazed with Palladium Alloys", Welding J 71 [1] (Jan 1992), pp. 25s-33s.
42. Kang, S., E.M. Dunn, J.H. Selverian, and H.J. Kim, "Issues in Ceramic-to-Metal Joining: An Investigation of Brazing a Silicon Nitride-Based Ceramic to a Low Expansion Superalloy", Ceram Bull 68 [9] (1989), pp. 1608-1617.
43. Naka, M., M. Tsuyoshi and I. Okamoto, "Ti-precoating effect on Wetting and Joining of Cu to SiC", ISIJ Int 30 [12] (1990), pp. 1108-1113.
44. Delanny, F., L. Froyen, and A. Deruyttere, "The Wetting of Solids by Molten Metals and its Relation to the Preparation of Metal-Matrix Composites", J Mat Sci 22 (1987), pp. 1-16.
45. Ohuchi, F.S. and Q. Zhong, "Electronic Structure of Metal-Ceramic Interfaces", ISIJ Int 30 [12] (1990), pp. 1059-1065.
46. Ohuchi F.S. and M. Kohyama, "Electronic Structure and Chemical Reactions and Metal-Alumina and Metal-Aluminum Nitride Interfaces" J Amer Ceram Soc 74 [6] (1991), pp. 1163-1187.
47. Nath, K. and A.B. Anderson, "Oxidative Bonding of (0001) α -Al₂O₃ to Close-Packed Surfaces of the First Transition Metal Series, Sc through Cu", Phys Rev B 39 [2] (15 Jan 1991), pp. 1013-1019.

48. Johnson, K.H., and S.V. Pepper, "Molecular-Orbital Model for Metal-Sapphire Interfacial Strength", J Appl Phys 53 (1982), pp. 6634-6637.
49. Li, J.G., "Wetting and Interfacial Bonding of Metals with Ionocovalnet Oxides", J Amer Ceram Soc 75 [11] (1992), pp. 3118-3126.
50. Ramsey, M.J. and M.H. Lewis, "Interfacial Reaction Mechanisms in Syalon Ceramic Bonding", Mat Sci and Eng 71 (1985), pp. 113-122.
51. Klomp, J.T., "Ceramic and Metal Surfaces in Ceramic-to-Metal Bonding", Brit Ceram Soc Proc 34 (Aug 1984), pp. 249-259.
52. Okamoto, T., "Interfacial Structure of Metal-Ceramic Joints", ISIJ Int 30 [12] (1990), pp. 1033-1040.
53. Naidich, Yu.V., "Wettability of Solids by Liquid Metals", Prog in Surf Membrane Sci 14 (1988), pp. 353,388.
54. Boadi, J.K., T. Yano and T. Iseki, "Brazing of Pressureless-Sintered SiC Using Ag-Cu-Ti Alloy", J Mater Sci 22 (1987), pp. 2431-2434.
55. Li, X.L., R. Hillel, F. Teyssandier, S.K. Choi, and F.J.J. Van Loo, "Reactions and Phase Relations in the Ti-Al-O System", Acta Met Mater 40 [11] (1992), pp. 3149-3157.
56. Hatakeyama, F., K. Sukanuma, and T. Okamoto, "Solid-State Bonding of Alumina to Austenitic Stainless Steel", J Mater Sci 21 (1986), pp. 2455-2461.
57. Tressler, R.E., T.L. Moore, and R.L. Crane, "Reactivity and Interface Characteristics of Titanium-Alumina Composites", J Mater Sci 8 (1973), pp. 151-161.
58. Naka, M., K. Asami, I Okamoto, and Y. Arata, "Intermediary Layer of Titanium Oxide in Al₂O₃/Cu Joints Using Amorphous Cu-Ti Filler Metals", Trans JWRI 12 [1] (1983), pp. 145-148.
59. Bang, K.S. and S. Liu, "Interfacial Reaction between Alumina and Cu-Ti Filler Metal during Reactive Metal Brazing", Welding J 73 [3] (1994), pp. 54s-60s.

60. Kim, D.H., S.H. Hwang, and S.S. Chun, "The Wetting, Reaction and Bonding of Silicon Nitride by Cu-Ti Alloys", J Mat Sci 26 (1991), pp. 3223-3234.
61. Whatley, W.J. and F.E. Wawner, "Kinetics of the Reaction Between SiC (SCS-6) Filaments and Ti(6Al-4V) Matrix", J Mater Sci Letters 4 (1985), pp. 173-175.
62. Kuzumaki, T., T. Ariga and Y. Miyamota, "Effect of Additional Elements in Ag-Cu Based Filler Metal on Brazing of Aluminum Nitride to Metals", ISIJ Int 30 [12] (1990), pp. 1135-1141.
63. Joshi, A., H.S. Hu, L. Jesion, J.J. Stephens, and J. Wadsworth, "High-Temperature Interactions of Refractory Metal Matrices with Selected Ceramic Reinforcements", Met Trans 21A (Nov 1990), pp. 2829-2837.
64. Torvund, T., O. Grong, O.M. Akelsen, J.H. Ulvensoen, "A Process Model for Active Brazing of Ceramics", J Mat Sci 31 (1996), pp. 6215-6222.
65. Wagner, C.Z., Z. Phys. Chem., 21 [25] (1933).
66. Birks, N., and G.H. Meier, Introduction to High Temperature Oxidation of Metals, Thomas Litho Ltd., East Kilbride, Scotland, (1983), pp. 41-45.
67. Fromhold, A.T., and Cook, E.L., J. Phys. Soc. Japan 48, (1980), pp. 2022-2028.
68. Baldwin, M.D., P.R. Chidambaram, and G.R. Edwards, "Spreading and Interlayer Formation at the Copper-Copper Oxide/Polycrystalline Alumina Interface" Met Trans 25A (November 1994), pp. 2497-2506.
69. Williams, D.S., R.A. Rapp, and J.P. Hirth, Metall. Trans. A 12A (1981) pp. 639-647.
70. Howe, J.M., "Bonding, Structure, and Properties of Metal/Ceramic Interfaces: Part 1 Chemical Bonding, Chemical Reaction, and Interfacial Structure" Int Mat Rev 38 [5] (1993), pp. 233-256.
71. Chidambaram, P.R., Ph.D. Thesis, "Thermodynamic and Kinetic Aspects of Reactive Metals in Contact with Aluminum Oxide", Colorado School of Mines, T-4319, December 1992.
72. Howe, J.M., Int. Mater. Rev. 38, (1993), pp. 233-256.

73. Elssner, G., T. Suga, and M. Turwitt, J. Physic 46 [4] (1985), p. 597.
74. Suga, T. and G Elssner, J. Physic 46 [4] (1985), p. 657.
75. Dekock, J.A. and Y.A. Chang, "The Stability of Interfaces in High-Temperature Metal-Matrix Composites", JOM (March 1993), pp. 21-23.
76. Chidambaram P.R., G.R. Edwards, and D.L. Olson, "Fundamental Issues Concerning the Microdesigning of Metal-eramic Interfaces", Composite Interfaces 2 (1993), pp. 127-140.
77. Oh, T.S., R.M. Cannon, and R.O. Ritchie, J. Am. Ceram. Soc. 70 (1987), p. 352.
78. Oh, T.S., J. Rodel, R.M. Cannon, and R.O. Ritchie, Acta Metall 36 (1988), p. 2083.
79. Suganuma, K., K. Niihara, T. Fujita, and T. Okamoto, in Proc. MRS Int. Meeting on 'Advanced Materials' Vol. 8, "Metal-Ceramic Joints" (ed. M. Doyama *et al.*), 113 (1989), Pittsburgh, PA, Materials Research Society.
80. Chidambaram, P.R., G.R. Edwards, and D.L. Olson, "Wetting of Ceramic by Molten etals : Rate Controlling Phenomena", The Metal Sci of Joining, Edited by M.J. Cieslak, J.H. Perepezko, S. Kang, and M.E. Glicksman, The Minerals, Metals, and Materials Society, 1992, pp. 67-71.
81. Duvall, D.S., W.A. Owczarski, and D.F. Paulonis, Weld. J. 53, (1974), pp. 203-214.
82. Moore, T.J. and J.M. Kalinowski, in MRS Symp. Proc. On 'High Temperature Ordered Intermetallic Alloys V' (ed. I. Baker *et al.*)288 (1993), pp. 1173-1178, Pittsburgh, PA, Materials Research Society.
83. Wells, R.R. and E.B. Mikus, "Thin film Diffusion Brazing of Titanium Members Using Copper Intermediaries", U.S. Patent 3 417 461. Northrop Hawthorne, CA (1968).
84. Komizo, Y., F. Kashimoto, T. Tomita, and K. Ogawa, Q. J. Jpn Weld. Soc. 8 (1990), pp. 197-204.

85. Eustathopoulos, N., J.C. Joud, P. Desre, and J.M. Hicter, "The Wetting of Carbon by Aluminum and Aluminum Alloys", J Mat Sci 9 (1974) pp. 1233-1242.